


Article

Sensorless Control of Seven-Phase PMSM Drives Using NSV-SVPWM with Minimum Current Distortion

Kamel Saleh ^{1,*}  and Mark Sumner ² 

¹ Electrical Engineering Department, Faculty of Engineering and Information Technology, New Campus, An-Najah National University, Nablus P.O. Box 7, Palestine

² Electrical and Electronic Engineering Department, Faculty of Engineering, University Park, University of Nottingham, Nottingham NG7 2RD, UK; mark.sumner@nottingham.ac.uk

* Correspondence: kamel.saleh@najah.edu

Abstract: This paper introduces three different algorithms to track the saliency in the seven-phase PMSM to obtain sensorless speed control. These algorithms are based on measuring the amount of change of the stator currents when different active vectors are implemented using the Near Six Vectors-Space Vector Pulse Width Modulation (NSV-SVPWM). Then, a comparison between these algorithms in terms of the Total Harmonics Distortion (THD) associated with implementing each algorithm is presented. The increase in the current distortion in these algorithms is related to the fact that narrow active vectors in these algorithms should be extended to t_{min} (8 μ s) for proper measurement in the current dynamics due to the oscillation in the currents. However, since the time duration of these active vectors in NSV-SVPWM will be 2.52 times longer than others, it is found that using these long active vectors will result in minimum current distortion. Simulation results are provided to investigate the effect of using the dynamic response of different active vectors on the THD of the current. Moreover, the results demonstrate the effectiveness of the proposed control technique to maintain the performance of the seven-phase PMSM motor drive post the failure in the speed sensor.



Citation: Saleh, K.; Sumner, M. Sensorless Control of Seven-Phase PMSM Drives Using NSV-SVPWM with Minimum Current Distortion. *Electronics* **2022**, *11*, 792. <https://doi.org/10.3390/electronics11050792>

Academic Editor: Teresa Orłowska-Kowalska

Received: 6 February 2022

Accepted: 25 February 2022

Published: 3 March 2022

Publisher's Note: MDPI stays neutral with regard to jurisdictional claims in published maps and institutional affiliations.



Copyright: © 2022 by the authors. Licensee MDPI, Basel, Switzerland. This article is an open access article distributed under the terms and conditions of the Creative Commons Attribution (CC BY) license (<https://creativecommons.org/licenses/by/4.0/>).

Keywords: sensorless; seven-phase motor; NSV-SVPWM; THD

1. Introduction

Multi-phase machines are becoming of increased interest in many industrial applications especially for medium- and high-power applications such as in marine, aerospace, and railway industries. This interest is related to the fact that the multi-phase machines offer some advantages over the three-phase drives. Firstly, it is possible to obtain a higher power rating motor without the need to increase the phase current or the voltage (same IGBT rating). Secondly, it helps to reduce the amplitude and increase the frequency of the torque ripple. Finally, it offers a high degree of reliability as it is inherently fault-tolerant [1,2].

In multi-phase motor drives, it is quite important that the output of the inverter will be purely sinusoidal because any 3rd, 5th, and 7th harmonic that exist in the output of the inverter will cause a huge stator current. For this reason, multi-dimensional SVPWM should be implemented instead of the 2D-SVPWM. The multi-dimensional SVPWM is based on the concept of orthogonal multi-dimensional vector space which can synthesize voltage vectors in multi d-q subspaces to generate a sinusoidal output voltage [3–9].

Most of the industrial drive systems use speed sensors (encoder or resolver) to obtain the rotor position and speed to achieve vector control of the PMSMs. Unfortunately, using these sensors will reduce the reliability of the whole drive system as these sensors interfere with the noise. Therefore, many researchers have been directed to the “sensorless” or “encoderless” control of the PMSM drive where the rotor position and speed are obtained without using encoders or resolvers [10–15].

Sensorless control of five-phase motors has been researched in the last couple of years. This research has focused on model-based sensorless control, direct torque control, and high-frequency injections [16–20]. Recently, a few papers were presented the sensorless control of seven-phase motors using model base methods [21–27]. To the authors’ best knowledge, no paper has introduced the sensorless control of the seven-phase motor based on high-frequency excitation.

This paper introduces a novel sensorless control technique of the seven-phase PMSM with minimum current distortion. The algorithm to obtain the speed and position of the rotor is based on measuring the amount of change of the stator currents when the inverter is switching using the NSV-SVPWM. The time duration of each switching action of the inverter varies according to the applied vector. By measuring the amount of change of the current when the long vectors are applied, the current distortion can be reduced significantly as there are not any extensions of the vectors.

2. Sensored Speed Control of the Seven-Phase PMSM

2.1. Overview of the Seven-Phase PMSM Model

Figure 1 illustrates the seven-phase PMSM drive topology. The dynamic model of the motor is given by Equations (1)–(3).

$$[V_s] = r_s * [I_s] + \Delta[\varphi_s] \tag{1}$$

where $[V_s] = [V_{sA}, V_{sB}, V_{sC}, V_{sD}, V_{sE}, V_{sF}, V_{sG}]^T$ are the stator applied voltages, $[I_s] = [i_{sA}, i_{sB}, i_{sC}, i_{sD}, i_{sE}, i_{sF}, i_{sG}]^T$ are the stator currents, $[\varphi_s] = [\varphi_{sA}, \varphi_{sB}, \varphi_{sC}, \varphi_{sD}, \varphi_{sE}, \varphi_{sF}, \varphi_{sG}]^T$ are the stator linkage fluxes, r_s is the stator resistance, and $\Delta = \frac{d}{dt}$.

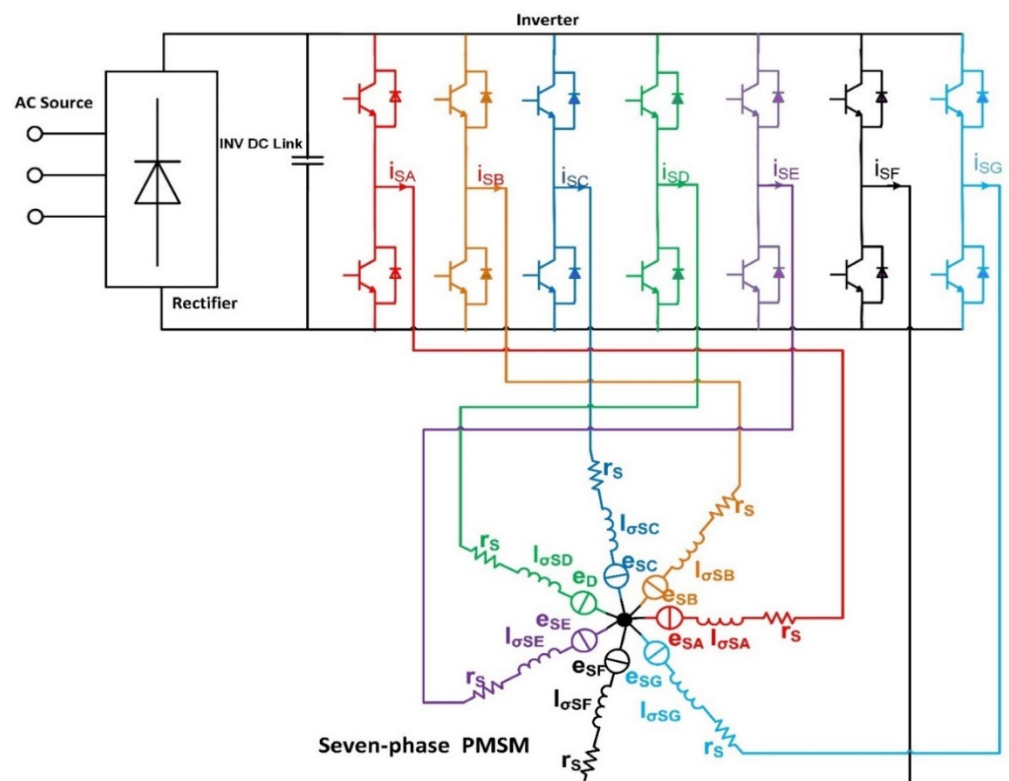


Figure 1. Seven-phase drive topology.

The stator linkage fluxes can be expressed as:

$$[\varphi_s] = L_{ms} * [I_s] + \varphi_M \tag{2}$$

$$\varphi_M = \lambda_m * \begin{bmatrix} \cos(\theta_R) \\ \cos(\theta_R - 2\pi/7) \\ \cos(\theta_R - 4\pi/7) \\ \cos(\theta_R - 6\pi/7) \\ \cos(\theta_R - 8\pi/7) \\ \cos(\theta_R - 10\pi/7) \\ \cos(\theta_R - 12\pi/7) \end{bmatrix} \tag{3}$$

where L_{ms} is the stator inductances matrix, λ_m is the peak permanent magnet flux linkage, and θ_R is the rotor position. The motor parameters that are used in this paper are given in the Appendix A.

2.2. Space Vector Distribution

The SVPWM technique that is used in three-phase PMSMs can't be implemented in seven-phase PMSMs, because the implementing of this SVPWM technique will generate 3rd and 5th harmonics at the output voltage of the inverter. This would produce large 3rd and 5th stator currents, and is related to the fact that these harmonics are limited by the stator impedance only due to the absence of the rotating back EMF [3–8]. Hence, to obtain pure sinusoidal currents in the seven-phase motor, the 3rd and 5th harmonics should be suppressed from the output of the inverter. This can be achieved using the NSV-SVPWM only. In this technique, reference voltage (V_{ref}), which is the output of the controller, is decoupled to three orthogonal planes. The first plane rotates at ω and is called the x1-y1 plane where ω is the synchronous speed of the motor. The second one rotates at 3ω and is called the x3-y3 plane. The final one rotates at 5ω and is called x5-y5, using Equations (4)–(6). This step is very important for identifying the 3rd and 5th harmonics in V_{ref} .

$$\begin{bmatrix} x1 \\ y1 \\ x3 \\ y3 \\ x5 \\ y5 \end{bmatrix} = [G] \begin{bmatrix} V_{sA} \\ V_{sB} \\ V_{sC} \\ V_{sD} \\ V_{sE} \\ V_{sF} \\ V_{sG} \end{bmatrix} \tag{4}$$

and

$$\begin{bmatrix} V_{sA} \\ V_{sB} \\ V_{sC} \\ V_{sD} \\ V_{sE} \\ V_{sF} \\ V_{sG} \end{bmatrix} = [G^{-1}] \begin{bmatrix} x1 \\ y1 \\ x3 \\ y3 \\ x5 \\ y5 \end{bmatrix} \tag{5}$$

where

$$G = \frac{2}{7} \begin{bmatrix} 1 & \cos(\frac{2\pi}{7}) & \cos(\frac{4\pi}{7}) & \cos(\frac{6\pi}{7}) & \cos(\frac{8\pi}{7}) & \cos(\frac{10\pi}{7}) & \cos(\frac{12\pi}{7}) \\ 0 & \sin(\frac{2\pi}{7}) & \sin(\frac{4\pi}{7}) & \sin(\frac{6\pi}{7}) & \sin(\frac{8\pi}{7}) & \sin(\frac{10\pi}{7}) & \sin(\frac{12\pi}{7}) \\ 1 & \cos 3(\frac{2\pi}{7}) & \cos 3(\frac{4\pi}{7}) & \cos 3(\frac{6\pi}{7}) & \cos 3(\frac{8\pi}{7}) & \cos 3(\frac{10\pi}{7}) & \cos 3(\frac{12\pi}{7}) \\ 0 & \sin 3(\frac{2\pi}{7}) & \sin 3(\frac{4\pi}{7}) & \sin 3(\frac{6\pi}{7}) & \sin 3(\frac{8\pi}{7}) & \sin 3(\frac{10\pi}{7}) & \sin 3(\frac{12\pi}{7}) \\ 1 & \cos 5(\frac{2\pi}{7}) & \cos 5(\frac{4\pi}{7}) & \cos 5(\frac{6\pi}{7}) & \cos 5(\frac{8\pi}{7}) & \cos 5(\frac{10\pi}{7}) & \cos 5(\frac{12\pi}{7}) \\ 0 & \sin 5(\frac{2\pi}{7}) & \sin 5(\frac{4\pi}{7}) & \sin 5(\frac{6\pi}{7}) & \sin 5(\frac{8\pi}{7}) & \sin 5(\frac{10\pi}{7}) & \sin 5(\frac{12\pi}{7}) \end{bmatrix} \tag{6}$$

The switching vectors V_{m1} , V_{m3} , and V_{m5} in the x_1 - y_1 plane, the x_3 - y_3 plane, and the x_5 - y_5 plane, respectively, can be calculated directly using Equation (7).

$$\begin{bmatrix} V_{m1} \\ V_{m3} \\ V_{m5} \end{bmatrix} = \frac{2}{7} * V_{DC} * \begin{bmatrix} 1 & e^{j\frac{2\pi}{7}} & e^{j\frac{4\pi}{7}} & e^{j\frac{6\pi}{7}} & e^{j\frac{8\pi}{7}} & e^{j\frac{10\pi}{7}} & e^{j\frac{12\pi}{7}} \\ 1 & e^{3j\frac{2\pi}{7}} & e^{3j\frac{4\pi}{7}} & e^{3j\frac{6\pi}{7}} & e^{3j\frac{8\pi}{7}} & e^{3j\frac{10\pi}{7}} & e^{3j\frac{12\pi}{7}} \\ 1 & e^{5j\frac{2\pi}{7}} & e^{5j\frac{4\pi}{7}} & e^{5j\frac{6\pi}{7}} & e^{5j\frac{8\pi}{7}} & e^{5j\frac{10\pi}{7}} & e^{5j\frac{12\pi}{7}} \end{bmatrix} \begin{bmatrix} Sw_A \\ Sw_B \\ Sw_C \\ Sw_D \\ Sw_E \\ Sw_F \\ Sw_G \end{bmatrix} \quad (7)$$

where V_{DC} is the DC link voltage, Sw_A , Sw_B , Sw_C , Sw_D , Sw_E , Sw_F , and Sw_G are the gating signals of upper switches of the phases ‘A’, ‘B’, ‘C’, ‘D’, ‘E’, ‘F’ and ‘G’, respectively, in the seven-phase inverter. According to the relational expression (7), the space vector distribution corresponding to the 128 switch states in Figure 2 can be obtained. These switching vectors have different amplitudes L1, L2, L3, L4, L5, L6. These amplitudes can be calculated using Equation (7) and given in Table 1.

Table 1. Switching vector amplitudes.

Vector Group Name	L1	L2	L3	L4	L5	L6	L7
amplitude	$0.127 \times V_{DC}$	$0.159 \times V_{DC}$	$0.229 \times V_{DC}$	$0.286 \times V_{DC}$	$0.356 \times V_{DC}$	$0.515 \times V_{DC}$	$0.642 \times V_{DC}$

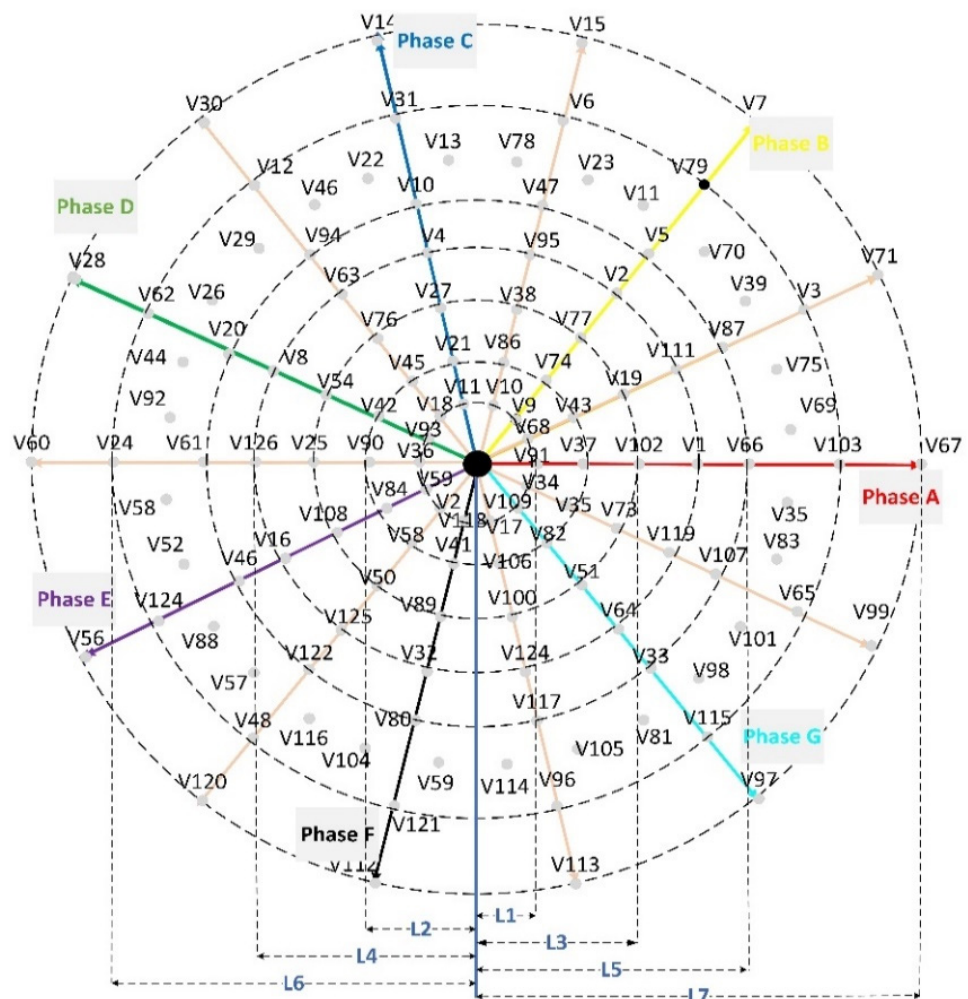


Figure 2. Voltage vector space distribution in the x_1 - y_1 plane.

2.3. NSV-SVPWM

Theoretically, the seven vector groups (L1, L2, L3, L4, L5, L6, and L7) can be used to generate the reference voltage. However, only the vectors L4, L6, and L7 are used to generate the reference vector in each sector practically. This is related to the fact that the vectors L1, L2, L3, and L5 are not continuous and their amplitude is small [3–8].

For example, if the reference voltage is located in the first sector: the six active vectors V1 (1000000), V3 (1100000), V67 (1100001), V71 (1110001), V103 (1110011), and V111 (1111011), in addition to the two null vectors V0 (0000000) and V127 (1111111), synthesize the reference voltages in x1-y1 plane as illustrated in Figure 3a and the associated PWM waveform will be as shown in Figure 3b.

The duration time for each vector can be calculated as:

$$\begin{bmatrix} t1 \\ t2 \\ t3 \\ t4 \\ t5 \\ t6 \end{bmatrix} = ts \times [T^{-1}] \begin{bmatrix} Vsref_x1 \\ Vsref_y1 \\ Vsref_x3 \\ Vsref_y3 \\ Vsref_x5 \\ Vsref_y5 \end{bmatrix} \tag{8}$$

where

$$T = \begin{bmatrix} L4 & L6 * \cos(\frac{2\pi}{7}) & L7 & L7 * \cos(\frac{2\pi}{7}) & L6 & L4 * \cos(\frac{2\pi}{7}) \\ 0 & L6 * \sin(\frac{2\pi}{7}) & 0 & L7 * \sin(\frac{2\pi}{7}) & 0 & L4 * \sin(\frac{2\pi}{7}) \\ L4 & L1 * \cos(\frac{3\pi}{7}) & -L3 & L3 * \cos(\frac{10\pi}{7}) & L1 & L4 * \cos(\frac{3\pi}{7}) \\ 0 & L1 * \sin(\frac{3\pi}{7}) & 0 & L3 * \sin(\frac{10\pi}{7}) & 0 & L4 * \sin(\frac{3\pi}{7}) \\ L4 & L5 * \cos(\frac{12\pi}{7}) & L2 & L2 * \cos(\frac{5\pi}{7}) & -L5 & L4 * \cos(\frac{5\pi}{7}) \\ 0 & L5 * \sin(\frac{12\pi}{7}) & 0 & L2 * \sin(\frac{5\pi}{7}) & 0 & L4 * \sin(\frac{5\pi}{7}) \end{bmatrix} \tag{9}$$

$$t0 = ts - t1 - t2 - t3 - t4 - t5 - t6 \tag{10}$$

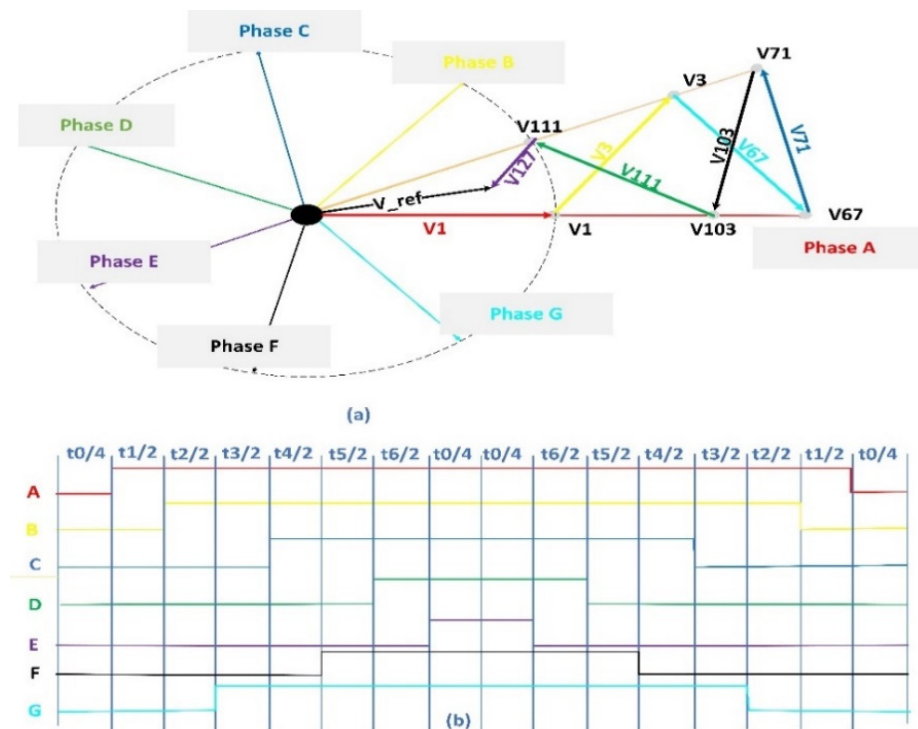


Figure 3. (a) NSV-SVPWM vector synthesis in x1-y1, (b) PWM waveform.

The algorithm to calculate the dwell time and the switching sequence in any sector k is shown in the flow chart in Figure 4.

where the $w1$, $w2$, and Table 2 are shown below:

$$w1 = \begin{bmatrix} L4 \cos((k-1)\frac{2\pi}{7}) & L6 \cos(k\frac{2\pi}{7}) & L7 \cos((k-1)\frac{2\pi}{7}) & L7 \cos(k\frac{2\pi}{7}) & L6 \cos((k-1)\frac{2\pi}{7}) & L4 \cos(k\frac{2\pi}{7}) \\ L4 \sin((k-1)\frac{2\pi}{7}) & L6 \sin(k\frac{2\pi}{7}) & L7 \sin((k-1)\frac{2\pi}{7}) & L7 \sin(k\frac{2\pi}{7}) & L6 \sin((k-1)\frac{2\pi}{7}) & L4 \sin(k\frac{2\pi}{7}) \\ L4 \cos(3(k-1)\frac{2\pi}{7}) & L1 \cos(3k\frac{2\pi}{7}) & -L3 \cos(3(k-1)\frac{2\pi}{7}) & -L3 \cos(3k\frac{2\pi}{7}) & L1 \cos(3(k-1)\frac{2\pi}{7}) & L4 \cos(3k\frac{2\pi}{7}) \\ L4 \sin(3(k-1)\frac{2\pi}{7}) & L1 \sin(3k\frac{2\pi}{7}) & -L3 \sin(3(k-1)\frac{2\pi}{7}) & -L3 \sin(3k\frac{2\pi}{7}) & L1 \sin(3(k-1)\frac{2\pi}{7}) & L4 \sin(3k\frac{2\pi}{7}) \\ L4 \cos(5(k-1)\frac{2\pi}{7}) & -L5 \cos(5k\frac{2\pi}{7}) & L2 \cos(5(k-1)\frac{2\pi}{7}) & L2 \cos(5k\frac{2\pi}{7}) & -L5 \cos(5(k-1)\frac{2\pi}{7}) & L4 \cos(5k\frac{2\pi}{7}) \\ L4 \sin(5(k-1)\frac{2\pi}{7}) & -L5 \sin(5k\frac{2\pi}{7}) & L2 \sin(5(k-1)\frac{2\pi}{7}) & L2 \sin(5k\frac{2\pi}{7}) & -L5 \sin(5(k-1)\frac{2\pi}{7}) & L4 \sin(5k\frac{2\pi}{7}) \end{bmatrix} \quad (11)$$

$$w2 = \begin{bmatrix} L4 \cos(k\frac{2\pi}{7}) & L6 \cos((k-1)\frac{2\pi}{7}) & L7 \cos(k\frac{2\pi}{7}) & L7 \cos((k-1)\frac{2\pi}{7}) & L6 \cos(k\frac{2\pi}{7}) & L4 \cos((k-1)\frac{2\pi}{7}) \\ L4 \sin(k\frac{2\pi}{7}) & L6 \sin((k-1)\frac{2\pi}{7}) & L7 \sin(k\frac{2\pi}{7}) & L7 \sin((k-1)\frac{2\pi}{7}) & L6 \sin(k\frac{2\pi}{7}) & L4 \sin((k-1)\frac{2\pi}{7}) \\ L4 \cos(3k\frac{2\pi}{7}) & L1 \cos(3(k-1)\frac{2\pi}{7}) & -L3 \cos(3k\frac{2\pi}{7}) & -L3 \cos(3(k-1)\frac{2\pi}{7}) & L1 \cos(3k\frac{2\pi}{7}) & L4 \cos(3(k-1)\frac{2\pi}{7}) \\ L4 \sin(3k\frac{2\pi}{7}) & L1 \sin(3(k-1)\frac{2\pi}{7}) & -L3 \sin(3k\frac{2\pi}{7}) & -L3 \sin(3(k-1)\frac{2\pi}{7}) & L1 \sin(3k\frac{2\pi}{7}) & L4 \sin(3(k-1)\frac{2\pi}{7}) \\ L4 \cos(5k\frac{2\pi}{7}) & -L5 \cos(5(k-1)\frac{2\pi}{7}) & L2 \cos(5k\frac{2\pi}{7}) & L2 \cos(5(k-1)\frac{2\pi}{7}) & -L5 \cos(5k\frac{2\pi}{7}) & L4 \cos(5(k-1)\frac{2\pi}{7}) \\ L4 \sin(5k\frac{2\pi}{7}) & -L5 \sin(5(k-1)\frac{2\pi}{7}) & L2 \sin(5k\frac{2\pi}{7}) & L2 \sin(5(k-1)\frac{2\pi}{7}) & -L5 \sin(5k\frac{2\pi}{7}) & L4 \sin(5(k-1)\frac{2\pi}{7}) \end{bmatrix} \quad (12)$$

It can be shown that if the 3rd and 5th harmonics of the stator currents are controlled to zero, i.e., the quantities V_{sref_x3} , V_{sref_y3} , V_{sref_x5} , V_{sref_y5} are set to zero as in most cases, Equation (10) yields the following [9]:

$$t2 = 1.8093 \times t1 \quad (13)$$

$$t3 = 2.2524 \times t1 \quad (14)$$

This ratio between the duration time of applying each vector is similar to the ratio of applied voltages $L4$, $L6$, and $L7$ found in Table 1. This result is quite important and will be used later on to compare different algorithms that are proposed in this paper to track the saturation saliency term of the current distortion.

The speed control of the seven-phase PMSM drive in sensed mode using the NSV-SVPWM technique has been simulated in saber according to the vector control structure depicted in Figure 5. It can be shown from the figure that the 3rd and 5th harmonics of the stator currents were controlled to zero by putting $id3_ref$, $iq3_ref$, $id5_ref$, and $iq5_ref$ to zero to obtain pure sinusoidal currents. The results of the simulation are shown in Figure 6.

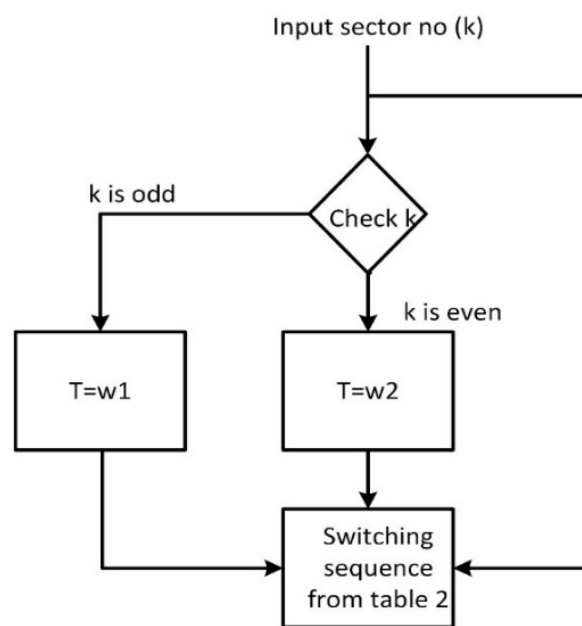


Figure 4. Algorithm to calculate dwell time and switching sequence in different sectors using NSV-SVPWM.

Table 2. Switching sequences in different sectors using NSV-SVPWM.

Sector No.	Q0	Q1	Q2	Q3	Q4	Q5	Q6	Q7
1	V0 (0000000)	V1 (1000000)	V3 (1100000)	V67 (1100001)	V71 (1110001)	V 103 (1110011)	V111 (1111011)	V127 (1111111)
2	V0 (0000000)	V2 (0100000)	V3 (1100000)	V7 (1110000)	V71 (1110001)	V79 (1111001)	V111 (1111011)	V127 (1111111)
3	V0 (0000000)	V2 (0100000)	V6 (0110000)	V7 (1110000)	V15 (1111000)	V79 (1111001)	V95 (1111101)	V127 (1111111)
4	V0 (0000000)	V4 (0010000)	V6 (0110000)	V14 (0111000)	V15 (1111000)	V 31 (1111100)	V95 (1111101)	V127 (1111111)
5	V0 (0000000)	V4 (0010000)	V12 (0011000)	V14 (0111000)	V30 (0111100)	V31 (1111100)	V63 (1111110)	V127 (1111111)
6	V0 (0000000)	V8 (0001000)	V12 (0011000)	V28 (0011100)	V30 (0111100)	V62 (0111110)	V63 (1111110)	V127 (1111111)
7	V0 (0000000)	V8 (0001000)	V24 (0001100)	V28 (0011100)	V60 (0011110)	V62 (0111110)	V126 (0111111)	V127 (1111111)
8	V0 (0000000)	V16 (0000100)	V24 (0001100)	V56 (0001110)	V60 (0011110)	V124 (0011111)	V126 (0111111)	V127 (1111111)
9	V0 (0000000)	V16 (0000100)	V48 (0000110)	V56 (0001110)	V120 (0001111)	V124 (0011111)	V125 (1011111)	V127 (1111111)
10	V0 (0000000)	V32 (0000010)	V48 (0000110)	V112 (0000111)	V120 (0001111)	V121 (1001111)	V125 (1011111)	V127 (1111111)
11	V0 (0000000)	V32 (0000010)	V96 (0000011)	V112 (0000111)	V113 (1000111)	V121 (1001111)	V124 (1101111)	V127 (1111111)
12	V0 (0000000)	V64 (0000001)	V96 (0000011)	V97 (1000011)	V113 (1000111)	V115 (1100111)	V124 (1101111)	V127 (1111111)
13	V0 (0000000)	V64 (0000001)	V65 (1000001)	V97 (1000011)	V99 (1100011)	V115 (1100111)	V119 (1110111)	V127 (1111111)
14	V0 (0000000)	V1 (1000000)	V65 (1000001)	V67 (1100001)	V99 (1100011)	V103 (1110011)	V119 (1110111)	V127 (1111111)

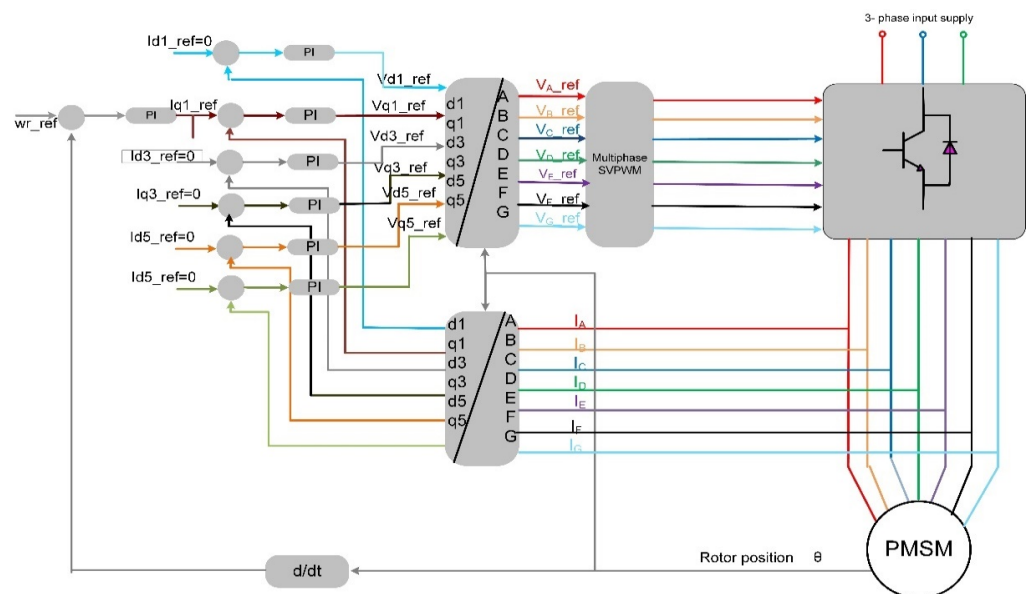


Figure 5. Vector control topology using NSV-SVPWM for the seven-phase drive.

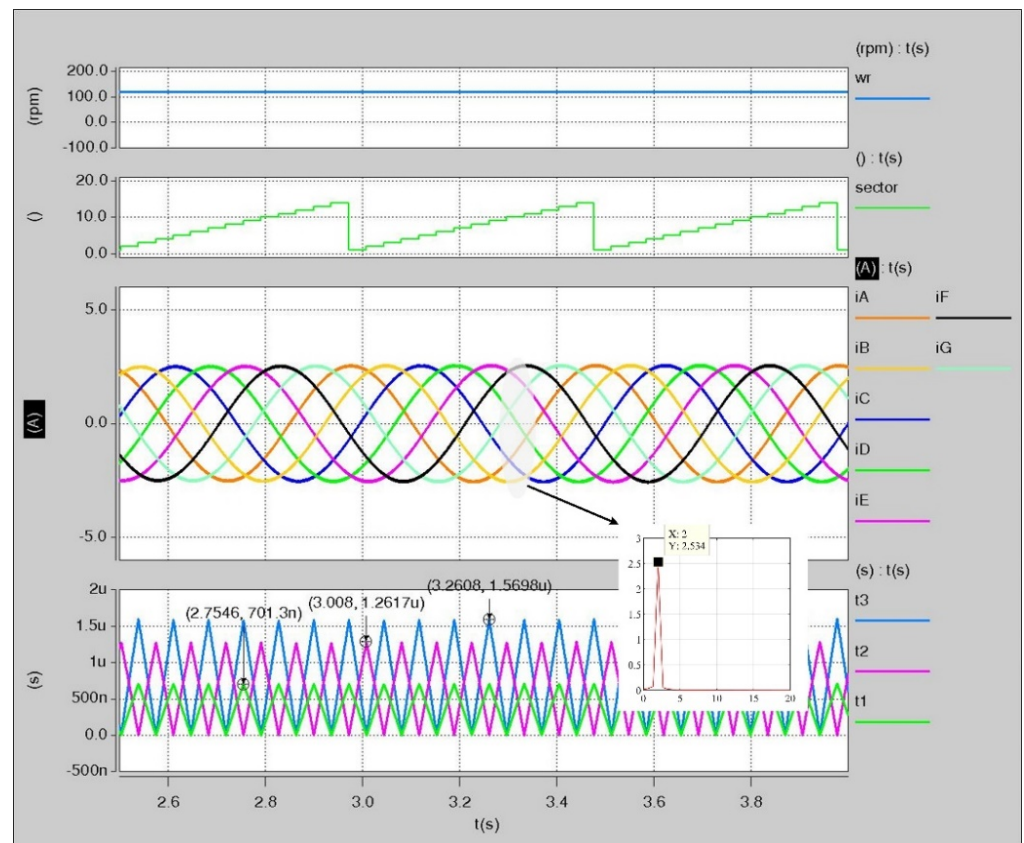


Figure 6. Sensored operation of the five phase motor.

It can be noticed from Figure 6 that motor speed was controlled to 120 rpm and the stator currents were distributed symmetrically and shifted by $(2\pi/7)$. Moreover, the spectrum of the stator currents shows that there are no 3rd and 5th harmonics in the stator currents as they are controlled to zero. It can be noticed also that the ratio between the duration of the applied vectors completely agrees with what is given in Equations (13) and (14).

3. Algorithms to Extract the Rotor Position in Seven-Phase PMSMs without Encoders

The inductances of the stator winding of the seven-phase PMSM are modulated by the saturation saliency of the main flux as shown in Equation (3), i.e., (the term $(2 * 2\pi/7)$). This modulation appears in the dynamic response of the stator currents of the seven-phase PMSM when any of the IGBTs in the inverter are switched on or off. Hence, the saliency position and the rotor position can be extracted by measuring the amount of change of the stator currents due to the IGBTs switching action in one PWM waveform. Moreover, since the NSV-SVPWM is used in this research, this will give flexibility in choosing the vector that will be used to track the saliency. In this paper, the first three active vectors Q1, Q2, and Q3 were used separately beside the null vector Q0 to track the saturation saliency as shown below.

3.1. Tracking Saliency Using the Active Vector Q1 (case = 0)

Figure 7a shows the PWM waveform in sector 1 obtained by implementing the NSV-SVPWM technique. Also, the figure illustrates the sampling time and the associated dynamic current responses obtained by applying the vectors Q1 and Q0. Figure 7b,c show the dynamic stator circuit of the PMSM when the vectors Q0 and Q1 are applied, respectively.

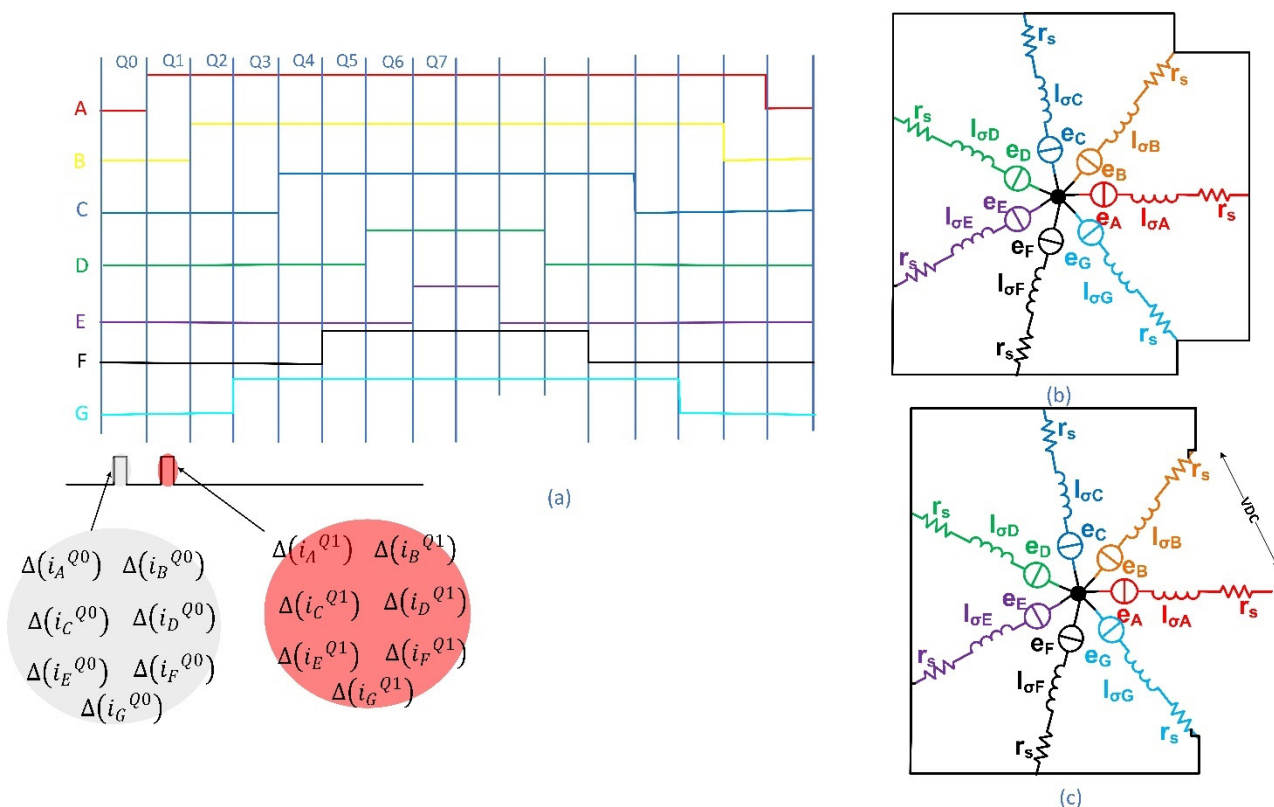


Figure 7. (a) Sampling instants of the current response when the vectors Q1 and Q0 are used to track the saliency, (b) dynamic circuit when Q0 is applied, and (c) dynamic circuit when Q1 is applied.

Using the circuits in Figure 7b,c the following equation holds true:

$$\begin{bmatrix} VDC \\ 0 \\ 0 \\ 0 \\ 0 \\ 0 \\ 0 \end{bmatrix} = r_s * \begin{bmatrix} i_A^{Q1} - i_A^{Q0} \\ i_B^{Q1} - i_B^{Q0} \\ i_C^{Q1} - i_C^{Q0} \\ i_D^{Q1} - i_D^{Q0} \\ i_E^{Q1} - i_E^{Q0} \\ i_F^{Q1} - i_F^{Q0} \\ i_G^{Q1} - i_G^{Q0} \end{bmatrix} + \begin{bmatrix} l_{\sigma A} * \Delta(i_A^{Q1} - i_A^{Q0}) \\ l_{\sigma B} * \Delta(i_B^{Q1} - i_B^{Q0}) \\ l_{\sigma C} * \Delta(i_C^{Q1} - i_C^{Q0}) \\ l_{\sigma D} * \Delta(i_D^{Q1} - i_D^{Q0}) \\ l_{\sigma E} * \Delta(i_E^{Q1} - i_E^{Q0}) \\ l_{\sigma F} * \Delta(i_F^{Q1} - i_F^{Q0}) \\ l_{\sigma G} * \Delta(i_G^{Q1} - i_G^{Q0}) \end{bmatrix} + \begin{bmatrix} e_A^{Q1} - e_A^{Q0} \\ e_B^{Q1} - e_B^{Q0} \\ e_C^{Q1} - e_C^{Q0} \\ e_D^{Q1} - e_D^{Q0} \\ e_E^{Q1} - e_E^{Q0} \\ e_F^{Q1} - e_F^{Q0} \\ e_G^{Q1} - e_G^{Q0} \end{bmatrix} \tag{15}$$

where l_{σ} is the stator leakage inductance and i_s is the back emf.

Equation (15) can be further simplified by neglecting the drop voltage on the r_s as it will be a very small quantity. By neglecting the back emf, there will be little change on it, hence Equation (16) can be obtained.

$$\begin{bmatrix} VDC \\ 0 \\ 0 \\ 0 \\ 0 \\ 0 \\ 0 \end{bmatrix} = \begin{bmatrix} l_{\sigma A} * \Delta(i_A^{Q1} - i_A^{Q0}) \\ l_{\sigma B} * \Delta(i_B^{Q1} - i_B^{Q0}) \\ l_{\sigma C} * \Delta(i_C^{Q1} - i_C^{Q0}) \\ l_{\sigma D} * \Delta(i_D^{Q1} - i_D^{Q0}) \\ l_{\sigma E} * \Delta(i_E^{Q1} - i_E^{Q0}) \\ l_{\sigma F} * \Delta(i_F^{Q1} - i_F^{Q0}) \\ l_{\sigma G} * \Delta(i_G^{Q1} - i_G^{Q0}) \end{bmatrix} \tag{16}$$

The position scalars p_{A_Q1} , p_{B_Q1} , p_{C_Q1} , p_{D_Q1} , p_{E_Q1} , p_{F_Q1} , and p_{G_Q1} can be constructed as follows:

$$\begin{bmatrix} p_{A_Q1} \\ p_{B_Q1} \\ p_{C_Q1} \\ p_{D_Q1} \\ p_{E_Q1} \\ p_{G_Q1} \\ p_{G_Q1} \end{bmatrix} = \begin{bmatrix} \Delta(i_A^{Q1} - i_A^{Q0}) \\ \Delta(i_C^{Q1} - i_C^{Q0}) \\ \Delta(i_E^{Q1} - i_E^{Q0}) \\ \Delta(i_G^{Q1} - i_G^{Q0}) \\ \Delta(i_B^{Q1} - i_B^{Q0}) \\ \Delta(i_D^{Q1} - i_D^{Q0}) \\ \Delta(i_F^{Q1} - i_F^{Q0}) \end{bmatrix} \tag{17}$$

The position scalars in other sectors are given in Table 3. These position scalars can be used to obtain p_alfa , p_beta as follows:

$$\begin{bmatrix} p_alfa \\ p_beta \end{bmatrix} = [V] \begin{bmatrix} p_{A_Q1} \\ p_{B_Q1} \\ p_{C_Q1} \\ p_{D_Q1} \\ p_{E_Q1} \\ p_{G_Q1} \\ p_{G_Q1} \end{bmatrix} \tag{18}$$

where

$$V = \begin{bmatrix} 1 & \cos(2\frac{2\pi}{7}) & \cos(4\frac{2\pi}{7}) & \cos(6\frac{2\pi}{7}) & \cos(8\frac{2\pi}{7}) & \cos(10\frac{2\pi}{7}) & \cos(12\frac{2\pi}{7}) \\ 1 & \sin(2\frac{2\pi}{7}) & \sin(4\frac{2\pi}{7}) & \sin(6\frac{2\pi}{7}) & \sin(8\frac{2\pi}{7}) & \sin(10\frac{2\pi}{7}) & \sin(12\frac{2\pi}{7}) \end{bmatrix} \tag{19}$$

Table 3. Saliency position scalars in each sector of the seven-phase PMSM using Q1 (case = 0).

Sector No.	$p_{A_Q1} = \Delta()$	$p_{B_Q1} = \Delta()$	$p_{C_Q1} = \Delta()$	$p_{D_Q1} = \Delta()$	$p_{E_Q1} = \Delta()$	$p_{F_Q1} = \Delta()$	$p_{G_Q1} = \Delta()$
1,14	$i_A^{Q1} - i_A^{Q0}$	$i_C^{Q1} - i_C^{Q0}$	$i_E^{Q1} - i_E^{Q0}$	$i_G^{Q1} - i_G^{Q0}$	$i_B^{Q1} - i_B^{Q0}$	$i_D^{Q1} - i_D^{Q0}$	$i_F^{Q1} - i_F^{Q0}$
2,3	$i_G^{Q1} - i_G^{Q0}$	$i_B^{Q1} - i_B^{Q0}$	$i_D^{Q1} - i_D^{Q0}$	$i_F^{Q1} - i_F^{Q0}$	$i_A^{Q1} - i_A^{Q0}$	$i_C^{Q1} - i_C^{Q0}$	$i_E^{Q1} - i_E^{Q0}$
4,5	$i_F^{Q1} - i_F^{Q0}$	$i_A^{Q1} - i_A^{Q0}$	$i_C^{Q1} - i_C^{Q0}$	$i_E^{Q1} - i_E^{Q0}$	$i_G^{Q1} - i_G^{Q0}$	$i_B^{Q1} - i_B^{Q0}$	$i_D^{Q1} - i_D^{Q0}$
6,7	$i_E^{Q1} - i_E^{Q0}$	$i_G^{Q1} - i_G^{Q0}$	$i_B^{Q1} - i_B^{Q0}$	$i_D^{Q1} - i_D^{Q0}$	$i_F^{Q1} - i_F^{Q0}$	$i_A^{Q1} - i_A^{Q0}$	$i_C^{Q1} - i_C^{Q0}$
8,9	$i_D^{Q1} - i_D^{Q0}$	$i_F^{Q1} - i_F^{Q0}$	$i_A^{Q1} - i_A^{Q0}$	$i_C^{Q1} - i_C^{Q0}$	$i_E^{Q1} - i_E^{Q0}$	$i_G^{Q1} - i_G^{Q0}$	$i_B^{Q1} - i_B^{Q0}$
10,11	$i_C^{Q1} - i_C^{Q0}$	$i_E^{Q1} - i_E^{Q0}$	$i_G^{Q1} - i_G^{Q0}$	$i_B^{Q1} - i_B^{Q0}$	$i_D^{Q1} - i_D^{Q0}$	$i_F^{Q1} - i_F^{Q0}$	$i_A^{Q1} - i_A^{Q0}$
12,13	$i_B^{Q1} - i_B^{Q0}$	$i_D^{Q1} - i_D^{Q0}$	$i_F^{Q1} - i_F^{Q0}$	$i_A^{Q1} - i_A^{Q0}$	$i_C^{Q1} - i_C^{Q0}$	$i_E^{Q1} - i_E^{Q0}$	$i_G^{Q1} - i_G^{Q0}$

The effectiveness of the saliency position tracking algorithm given in Table 3 is achieved using the vector control structure shown in Figure 8. The mechanical observer [27] is used to tune the noise in the position signals. The whole control structure has been simulated using a Saber modeling environment. Note that the simulation includes a minimum pulse-width of 10 us when di/dt measurements are made.

The results shown in Figure 9 prove the effectiveness of the proposed saliency tracking algorithm. The motor speed was controlled at 120 rpm under full load conditions. The dynamic response of applying the active vector Q1 was used to track the saliency. The results demonstrate that the proposed algorithms can track the saturation saliency (2x f_e) at low and zero speeds efficiently.

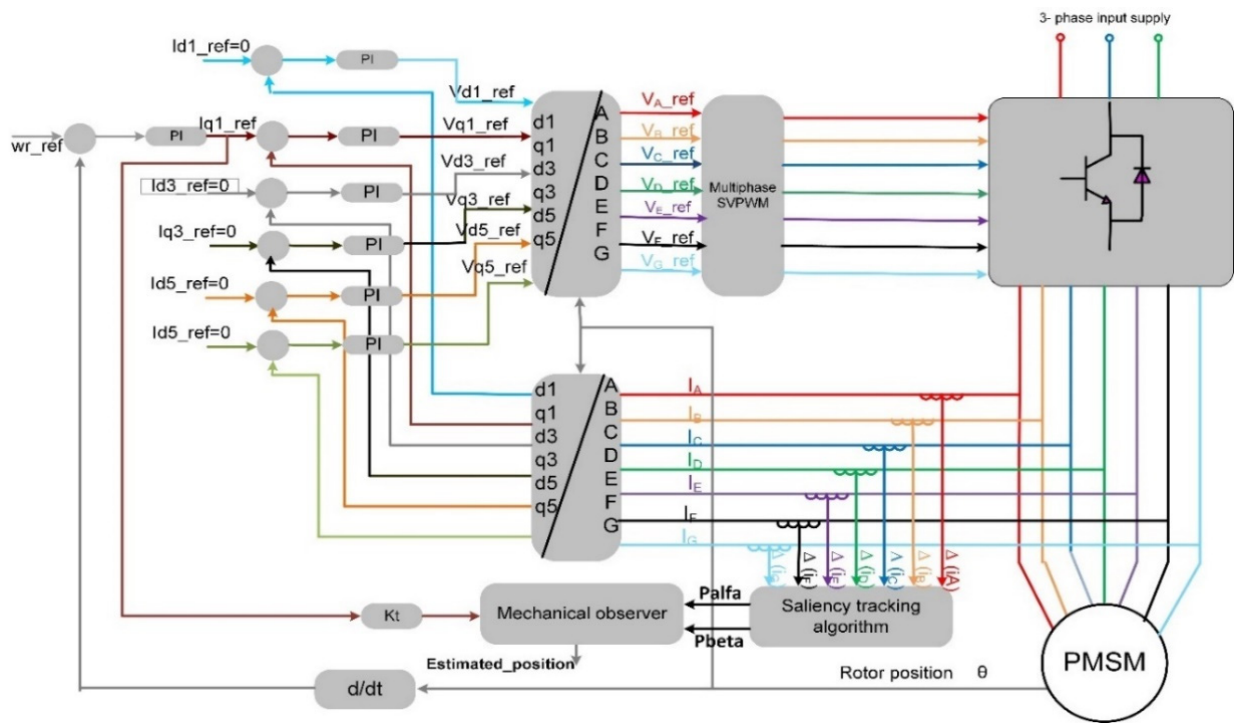


Figure 8. Control structure to obtain the saliency position in the seven-phase drive.

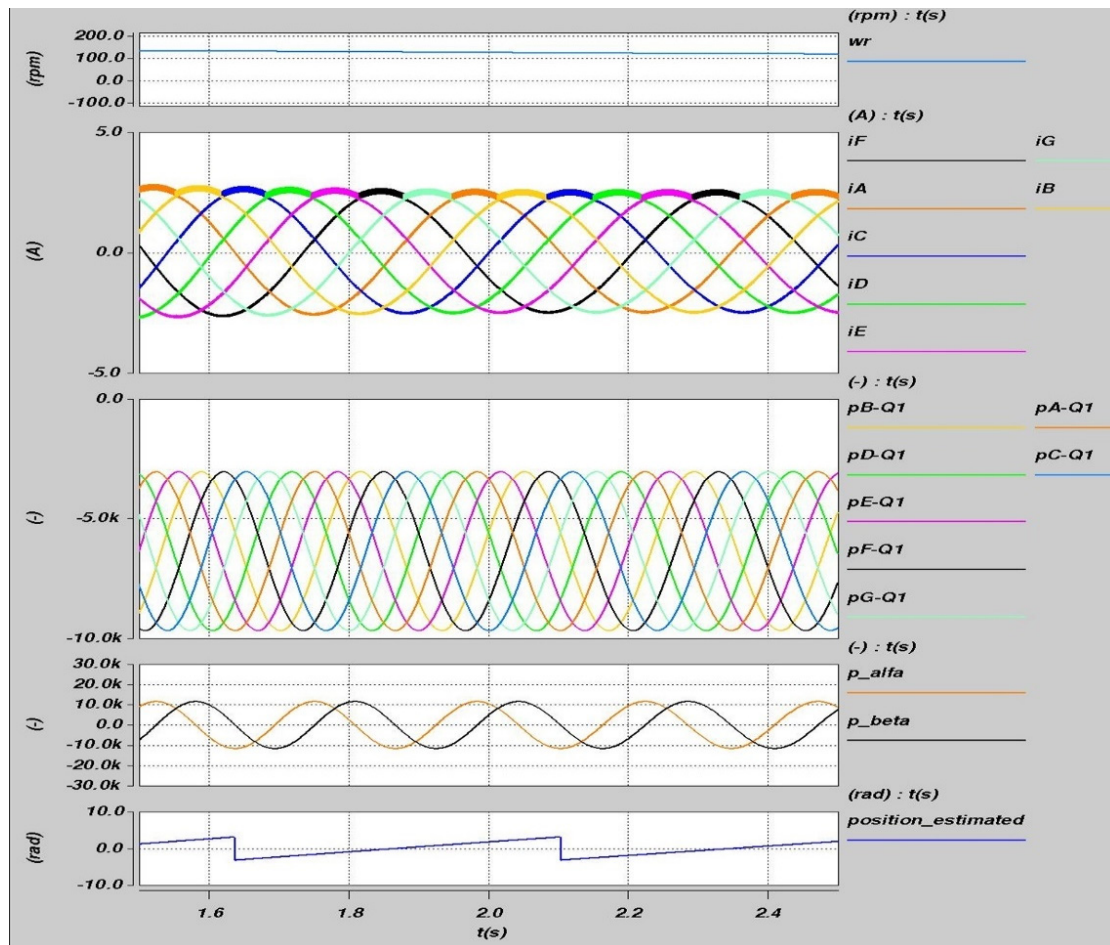


Figure 9. Saliency tracking results using the active vector Q1 (case = 0).

3.2. Tracking Saliency Using the Active Vectors Q2 and Q0 (case = 1)

Figure 10a shows the PWM waveform in Sector 1 obtained by implementing the NSV-SVPWM technique. The figure also illustrates the sampling time and the associated dynamic current responses obtained by applying the vectors Q2 and Q0. Figure 10b,c show the dynamic stator circuit of the PMSM when the vectors Q0 and Q2 are applied respectively.

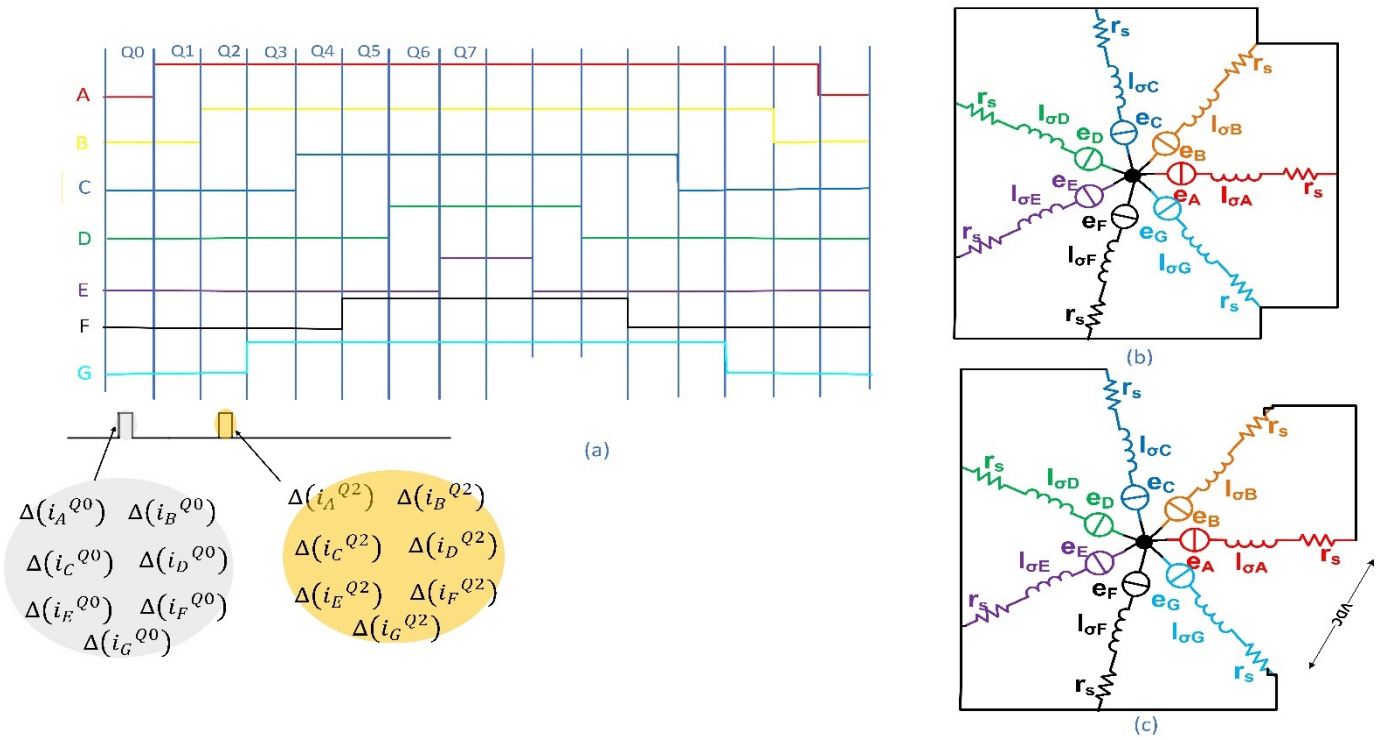


Figure 10. (a) Sampling instants when the current response of applying Q2 and Q0 are used to track the saliency, (b) dynamic circuit when Q0 is applied, and (c) dynamic circuit when Q2 is applied.

Using the circuit in Figure 10b,c the following equation hold true:

$$\begin{bmatrix} VDC \\ VDC \\ 0 \\ 0 \\ 0 \\ 0 \\ 0 \end{bmatrix} = r_s * \begin{bmatrix} i_A^{Q2} - i_A^{Q0} \\ i_B^{Q2} - i_B^{Q0} \\ i_C^{Q2} - i_C^{Q0} \\ i_D^{Q2} - i_D^{Q0} \\ i_E^{Q2} - i_E^{Q0} \\ i_F^{Q2} - i_F^{Q0} \\ i_G^{Q2} - i_G^{Q0} \end{bmatrix} + \begin{bmatrix} l_{\sigma A} * \Delta(i_A^{Q2} - i_A^{Q0}) \\ l_{\sigma B} * \Delta(i_B^{Q2} - i_B^{Q0}) \\ l_{\sigma C} * \Delta(i_C^{Q2} - i_C^{Q0}) \\ l_{\sigma D} * \Delta(i_D^{Q2} - i_D^{Q0}) \\ l_{\sigma E} * \Delta(i_E^{Q2} - i_E^{Q0}) \\ l_{\sigma F} * \Delta(i_F^{Q2} - i_F^{Q0}) \\ l_{\sigma G} * \Delta(i_G^{Q2} - i_G^{Q0}) \end{bmatrix} + \begin{bmatrix} e_A^{Q2} - e_A^{Q0} \\ e_B^{Q2} - e_B^{Q0} \\ e_C^{Q2} - e_C^{Q0} \\ e_D^{Q2} - e_D^{Q0} \\ e_E^{Q2} - e_E^{Q0} \\ e_F^{Q2} - e_F^{Q0} \\ e_G^{Q2} - e_G^{Q0} \end{bmatrix} \quad (20)$$

Using the same assumption applied before and related to the drop voltage on the r_s and the back emf, Equation (21) can be obtained.

$$\begin{bmatrix} VDC \\ VDC \\ 0 \\ 0 \\ 0 \\ 0 \\ 0 \end{bmatrix} = \begin{bmatrix} l_{\sigma A} * \Delta(i_A^{Q2} - i_A^{Q0}) \\ l_{\sigma B} * \Delta(i_B^{Q2} - i_B^{Q0}) \\ l_{\sigma C} * \Delta(i_C^{Q2} - i_C^{Q0}) \\ l_{\sigma D} * \Delta(i_D^{Q2} - i_D^{Q0}) \\ l_{\sigma E} * \Delta(i_E^{Q2} - i_E^{Q0}) \\ l_{\sigma F} * \Delta(i_F^{Q2} - i_F^{Q0}) \\ l_{\sigma G} * \Delta(i_G^{Q2} - i_G^{Q0}) \end{bmatrix} \quad (21)$$

The position scalars p_{A_Q2} , p_{B_Q2} , p_{C_Q2} , p_{D_Q2} , p_{E_Q2} , p_{F_Q2} , and p_{G_Q2} can be constructed as follows:

$$\begin{bmatrix} p_{A_Q2} \\ p_{B_Q2} \\ p_{C_Q2} \\ p_{D_Q2} \\ p_{E_Q2} \\ p_{F_Q2} \\ p_{G_Q2} \end{bmatrix} = \begin{bmatrix} -\Delta(i_D^{Q2} - i_D^{Q0}) \\ -\Delta(i_F^{Q2} - i_F^{Q0}) \\ -\Delta(i_A^{Q2} - i_A^{Q0}) \\ -\Delta(i_C^{Q2} - i_C^{Q0}) \\ -\Delta(i_E^{Q2} - i_E^{Q0}) \\ -\Delta(i_G^{Q2} - i_G^{Q0}) \\ -\Delta(i_B^{Q2} - i_B^{Q0}) \end{bmatrix} \tag{22}$$

The position scalars in other sectors are given in Table 4.

Table 4. Saliency position scalars in each sector of the seven-phase PMSMs using Q2 (case = 1).

Sector No.	$p_{A_Q2} = \Delta()$	$p_{B_Q2} = \Delta()$	$p_{C_Q2} = \Delta()$	$p_{D_Q2} = \Delta()$	$p_{E_Q2} = \Delta()$	$p_{F_Q2} = \Delta()$	$p_{G_Q2} = \Delta()$
1,2	$i_D^{Q2} - i_D^{Q0}$	$i_F^{Q2} - i_F^{Q0}$	$i_A^{Q2} - i_A^{Q0}$	$i_C^{Q2} - i_C^{Q0}$	$i_E^{Q2} - i_E^{Q0}$	$i_G^{Q2} - i_G^{Q0}$	$i_B^{Q2} - i_B^{Q0}$
3,4	$i_C^{Q2} - i_C^{Q0}$	$i_E^{Q2} - i_E^{Q0}$	$i_G^{Q2} - i_G^{Q0}$	$i_B^{Q2} - i_B^{Q0}$	$i_D^{Q2} - i_D^{Q0}$	$i_F^{Q2} - i_F^{Q0}$	$i_A^{Q2} - i_A^{Q0}$
5,6	$i_B^{Q2} - i_B^{Q0}$	$i_D^{Q2} - i_D^{Q0}$	$i_F^{Q2} - i_F^{Q0}$	$i_A^{Q2} - i_A^{Q0}$	$i_C^{Q2} - i_C^{Q0}$	$i_E^{Q2} - i_E^{Q0}$	$i_G^{Q2} - i_G^{Q0}$
7,8	$i_A^{Q2} - i_A^{Q0}$	$i_C^{Q2} - i_C^{Q0}$	$i_E^{Q2} - i_E^{Q0}$	$i_G^{Q2} - i_G^{Q0}$	$i_B^{Q2} - i_B^{Q0}$	$i_D^{Q2} - i_D^{Q0}$	$i_F^{Q2} - i_F^{Q0}$
9,10	$i_G^{Q2} - i_G^{Q0}$	$i_B^{Q2} - i_B^{Q0}$	$i_D^{Q2} - i_D^{Q0}$	$i_F^{Q2} - i_F^{Q0}$	$i_A^{Q2} - i_A^{Q0}$	$i_C^{Q2} - i_C^{Q0}$	$i_E^{Q2} - i_E^{Q0}$
11,12	$i_F^{Q2} - i_F^{Q0}$	$i_A^{Q2} - i_A^{Q0}$	$i_C^{Q2} - i_C^{Q0}$	$i_E^{Q2} - i_E^{Q0}$	$i_G^{Q2} - i_G^{Q0}$	$i_B^{Q2} - i_B^{Q0}$	$i_D^{Q2} - i_D^{Q0}$
13,14	$i_E^{Q2} - i_E^{Q0}$	$i_G^{Q2} - i_G^{Q0}$	$i_B^{Q2} - i_B^{Q0}$	$i_D^{Q2} - i_D^{Q0}$	$i_F^{Q2} - i_F^{Q0}$	$i_A^{Q2} - i_A^{Q0}$	$i_C^{Q2} - i_C^{Q0}$

The effectiveness of the saliency position tracking algorithm given in Table 4 is achieved using the vector control structure shown in Figure 8. The results shown in Figure 11 prove the effectiveness of the proposed saliency tracking algorithm. The motor speed was controlled at 120 rpm under full load conditions. The dynamic response of applying the active vector Q2 was used to track the saliency. The results demonstrate that the proposed algorithms could track the saturation saliency (2x τ_e) at low and zero speeds efficiently.

3.3. Tracking Saliency Using the Active Vectors Q3 and Q0 (case = 2)

Figure 12a shows the PWM waveform in Sector 1 obtained by implementing the NSV-SVPWM technique. Also, the figure illustrates the sampling time and the associated dynamic current responses obtained by applying the vectors Q3 and Q0. Figure 12b,c show the dynamic stator circuit of the PMSM when the vectors Q0 and Q3 are applied, respectively.

Using the circuit in Figure 12b,c, the following equation holds true:

$$\begin{bmatrix} VDC \\ VDC \\ VDC \\ 0 \\ 0 \\ 0 \\ 0 \end{bmatrix} = r_s * \begin{bmatrix} i_A^{Q3} - i_A^{Q0} \\ i_B^{Q3} - i_B^{Q0} \\ i_C^{Q3} - i_C^{Q0} \\ i_D^{Q3} - i_D^{Q0} \\ i_E^{Q3} - i_E^{Q0} \\ i_F^{Q3} - i_F^{Q0} \\ i_G^{Q3} - i_G^{Q0} \end{bmatrix} + \begin{bmatrix} l_{\sigma A} * \Delta(i_A^{Q3} - i_A^{Q0}) \\ l_{\sigma B} * \Delta(i_B^{Q3} - i_B^{Q0}) \\ l_{\sigma C} * \Delta(i_C^{Q3} - i_C^{Q0}) \\ l_{\sigma D} * \Delta(i_D^{Q3} - i_D^{Q0}) \\ l_{\sigma E} * \Delta(i_E^{Q3} - i_E^{Q0}) \\ l_{\sigma F} * \Delta(i_F^{Q3} - i_F^{Q0}) \\ l_{\sigma G} * \Delta(i_G^{Q3} - i_G^{Q0}) \end{bmatrix} + \begin{bmatrix} e_A^{Q3} - e_A^{Q0} \\ e_B^{Q3} - e_B^{Q0} \\ e_C^{Q3} - e_C^{Q0} \\ e_D^{Q3} - e_D^{Q0} \\ e_E^{Q3} - e_E^{Q0} \\ e_F^{Q3} - e_F^{Q0} \\ e_G^{Q3} - e_G^{Q0} \end{bmatrix} \tag{23}$$

Using the same assumption applied before and related to the drop voltage on the r_s and the bac emf, Equation (24) can be obtained.

$$\begin{bmatrix} VDC \\ VDC \\ VDC \\ 0 \\ 0 \\ 0 \\ 0 \end{bmatrix} = \begin{bmatrix} l_{\sigma A} * \Delta(i_A^{Q3} - i_A^{Q0}) \\ l_{\sigma B} * \Delta(i_B^{Q3} - i_B^{Q0}) \\ l_{\sigma C} * \Delta(i_C^{Q3} - i_C^{Q0}) \\ l_{\sigma D} * \Delta(i_D^{Q3} - i_D^{Q0}) \\ l_{\sigma E} * \Delta(i_E^{Q3} - i_E^{Q0}) \\ l_{\sigma F} * \Delta(i_F^{Q3} - i_F^{Q0}) \\ l_{\sigma G} * \Delta(i_G^{Q3} - i_G^{Q0}) \end{bmatrix} \tag{24}$$

The position scalars p_{A-Q3} , p_{B-Q3} , p_{C-Q3} , p_{D-Q3} , p_{E-Q3} , p_{F-Q3} , and p_{G-Q3} can be constructed as follows:

$$\begin{bmatrix} p_{A-Q3} \\ p_{B-Q3} \\ p_{C-Q3} \\ p_{D-Q3} \\ p_{E-Q3} \\ p_{F-Q3} \\ p_{G-Q3} \end{bmatrix} = \begin{bmatrix} \Delta(i_A^{Q3} - i_A^{Q0}) \\ \Delta(i_C^{Q3} - i_C^{Q0}) \\ \Delta(i_E^{Q3} - i_E^{Q0}) \\ \Delta(i_G^{Q3} - i_G^{Q0}) \\ \Delta(i_B^{Q3} - i_B^{Q0}) \\ \Delta(i_D^{Q3} - i_D^{Q0}) \\ \Delta(i_F^{Q3} - i_F^{Q0}) \end{bmatrix} \tag{25}$$

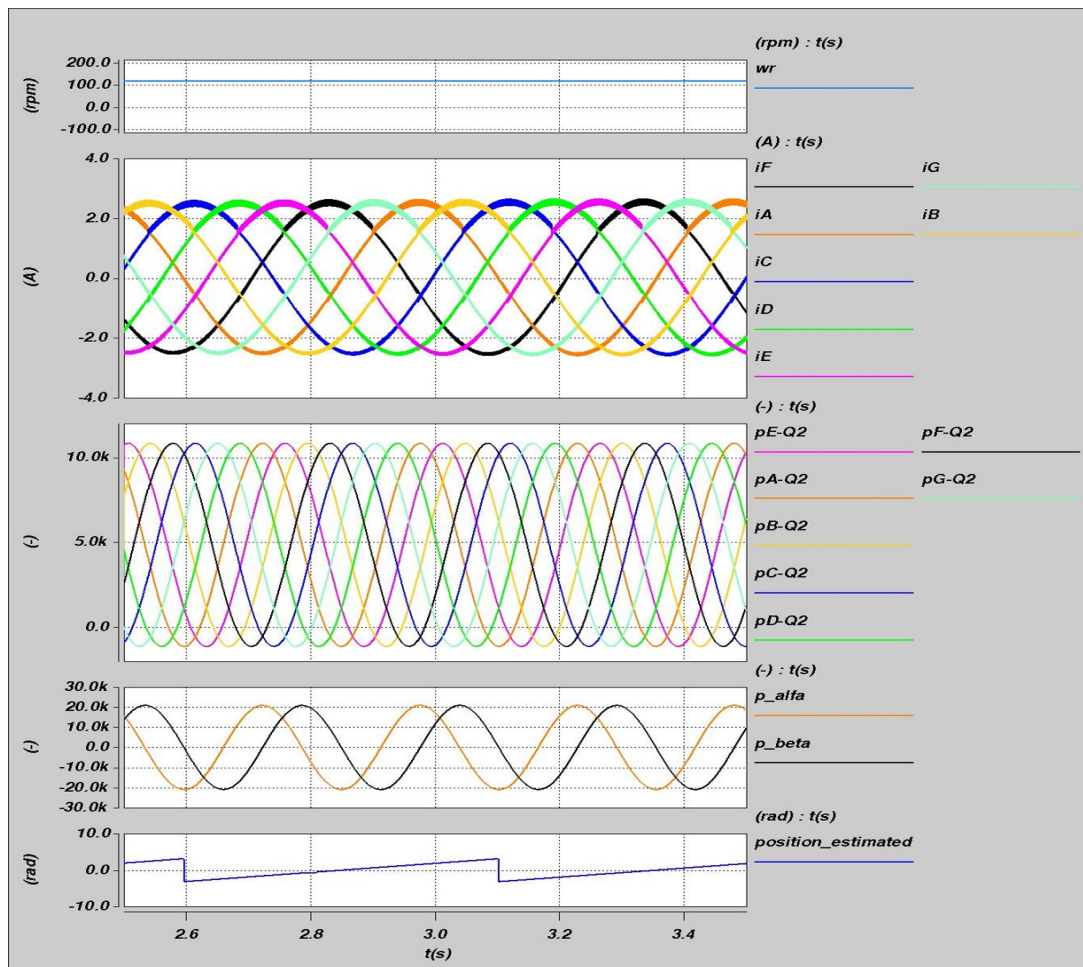


Figure 11. Saliency tracking results using the active vector Q2 (case = 1).

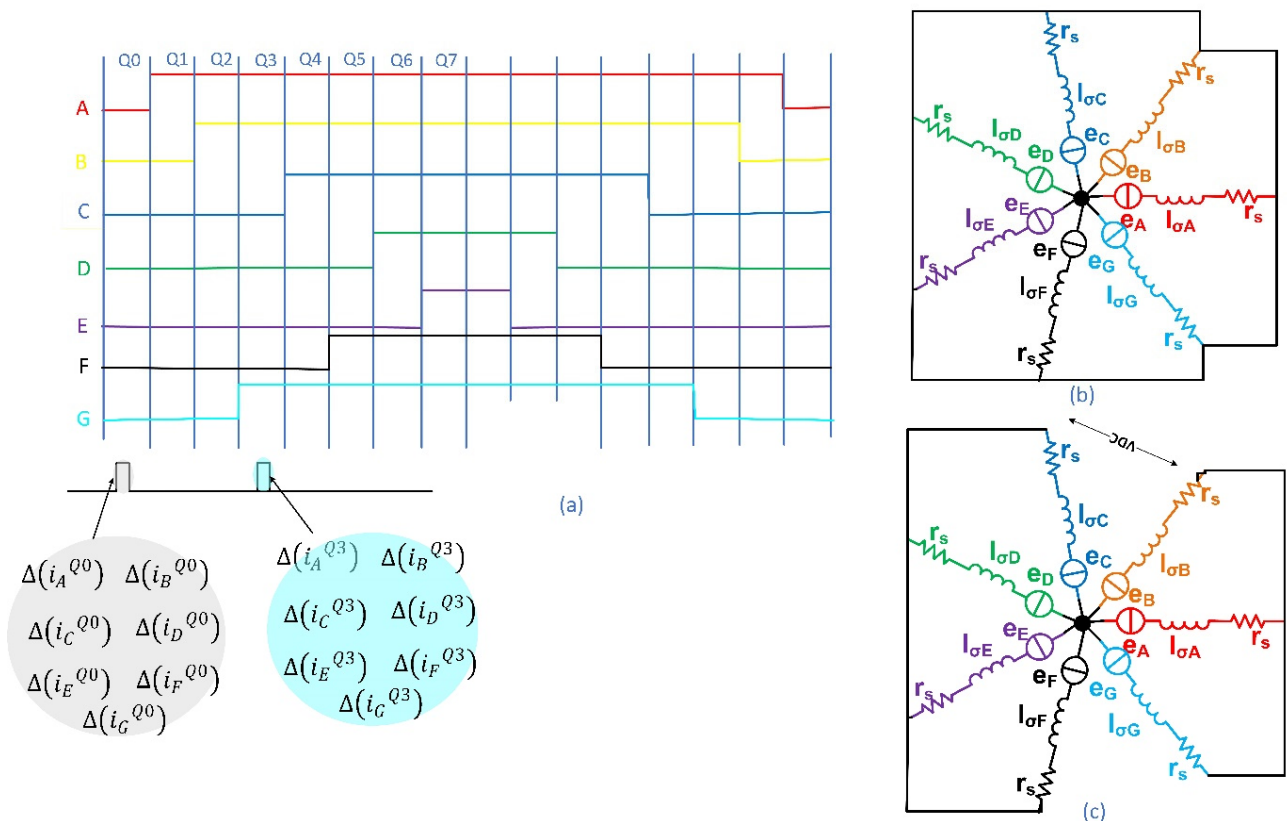


Figure 12. (a) Sampling instants when the current response of applying Q3 and Q0 are used to track the saliency, (b) dynamic circuit when Q0 is applied, and (c) dynamic circuit when Q3 is applied.

The position scalars in other sectors are given in Table 5.

Table 5. Saliency position scalars in each sector of the seven-phase PMSM using Q3 (case = 2).

Sector No.	$p_{A-Q3} = \Delta()$	$p_{B-Q3} = \Delta()$	$p_{C-Q3} = \Delta()$	$p_{D-Q3} = \Delta()$	$p_{E-Q3} = \Delta()$	$p_{F-Q3} = \Delta()$	$p_{G-Q3} = \Delta()$
1,14	$i_A^{Q3} - i_A^{Q0}$	$i_C^{Q3} - i_C^{Q0}$	$i_E^{Q3} - i_E^{Q0}$	$i_G^{Q3} - i_G^{Q0}$	$i_B^{Q3} - i_B^{Q0}$	$i_D^{Q3} - i_D^{Q0}$	$i_F^{Q3} - i_F^{Q0}$
2,3	$i_G^{Q3} - i_G^{Q0}$	$i_B^{Q3} - i_B^{Q0}$	$i_D^{Q3} - i_D^{Q0}$	$i_F^{Q3} - i_F^{Q0}$	$i_A^{Q3} - i_A^{Q0}$	$i_C^{Q3} - i_C^{Q0}$	$i_E^{Q3} - i_E^{Q0}$
4,5	$i_F^{Q3} - i_F^{Q0}$	$i_A^{Q3} - i_A^{Q0}$	$i_C^{Q3} - i_C^{Q0}$	$i_E^{Q3} - i_E^{Q0}$	$i_G^{Q3} - i_G^{Q0}$	$i_B^{Q3} - i_B^{Q0}$	$i_D^{Q3} - i_D^{Q0}$
6,7	$i_E^{Q3} - i_E^{Q0}$	$i_G^{Q3} - i_G^{Q0}$	$i_B^{Q3} - i_B^{Q0}$	$i_D^{Q3} - i_D^{Q0}$	$i_F^{Q3} - i_F^{Q0}$	$i_A^{Q3} - i_A^{Q0}$	$i_C^{Q3} - i_C^{Q0}$
8,9	$i_D^{Q3} - i_D^{Q0}$	$i_F^{Q3} - i_F^{Q0}$	$i_A^{Q3} - i_A^{Q0}$	$i_C^{Q3} - i_C^{Q0}$	$i_E^{Q3} - i_E^{Q0}$	$i_G^{Q3} - i_G^{Q0}$	$i_B^{Q3} - i_B^{Q0}$
10,11	$i_C^{Q3} - i_C^{Q0}$	$i_E^{Q3} - i_E^{Q0}$	$i_G^{Q3} - i_G^{Q0}$	$i_B^{Q3} - i_B^{Q0}$	$i_D^{Q3} - i_D^{Q0}$	$i_F^{Q3} - i_F^{Q0}$	$i_A^{Q3} - i_A^{Q0}$
12,13	$i_B^{Q3} - i_B^{Q0}$	$i_D^{Q3} - i_D^{Q0}$	$i_F^{Q3} - i_F^{Q0}$	$i_A^{Q3} - i_A^{Q0}$	$i_C^{Q3} - i_C^{Q0}$	$i_E^{Q3} - i_E^{Q0}$	$i_G^{Q3} - i_G^{Q0}$

The effectiveness of the saliency position tracking algorithm given in Table 5 is achieved using the vector control structure shown in Figure 8. The results shown in Figure 13 prove the effectiveness of the proposed saliency tracking algorithm. The motor speed was controlled at 120 rpm under full load conditions. The dynamic response of applying the active vector Q2 was used to track the saliency. The results demonstrate that the proposed algorithms could track the saturation saliency (2x σ_e) at low and zero speeds efficiently.

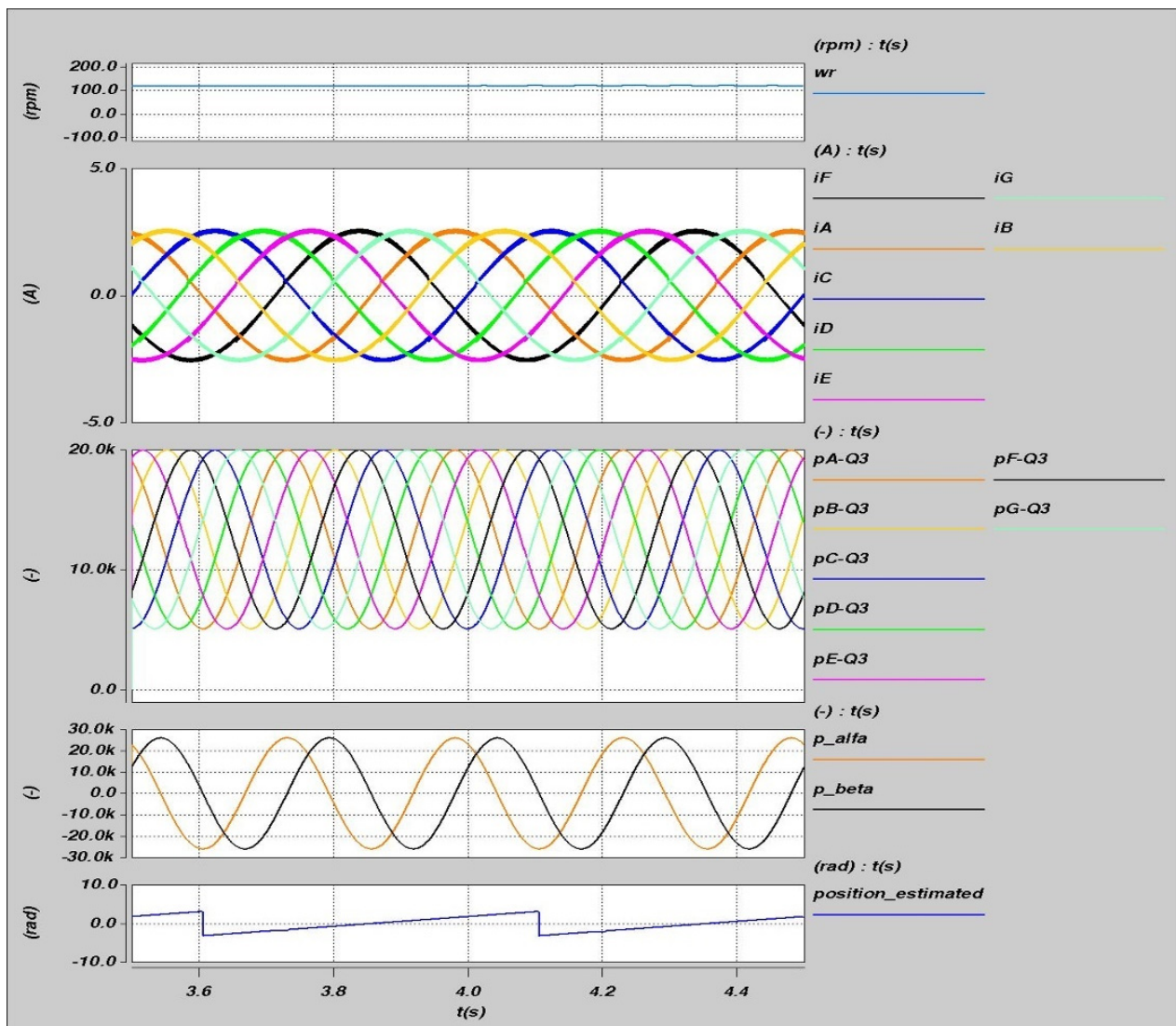


Figure 13. Saliency tracking results using active vector Q3 (case = 2).

4. Sensorless Control

The sensorless speed control structure of the seven-phase PMSM machine drive has been simulated using Saber modeling environment. The saliency tracking algorithm besides the mechanical observer was used to obtain the rotor position and the speed of the motor. These signals were then used to obtain field-oriented sensorless speed control of the seven-phase PMSM drive as shown in Figure 14.

Figure 15 shows the results of sensorless control of the seven-phase PMSM motor drive. The motor was working at a speed of 150 rpm and full load in sensorless mode. The algorithm given in Table 3 (case = 0) was used to track the saliency. Then, at time $t = 3$ s, the reference speed was changed from 150 rpm to 0 rpm. Finally, at $t = 5$ s, the reference speed was change from 0 rpm to -30 rpm. The results in Figure 15 shows that the motor maintained the performance post the failure in the speed sensor. Moreover, the transient and steady-state response of the system post the failure in the speed sensor was good as that before the failure.

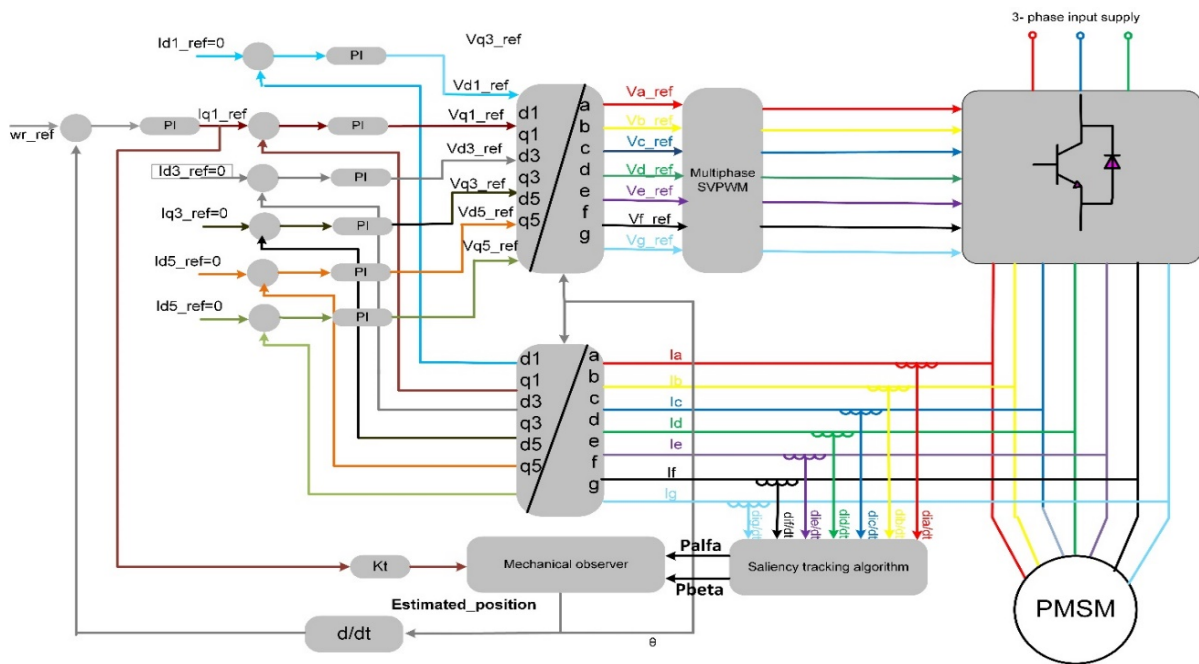


Figure 14. Speed control structure for the five-phase inverter PMSM drive post the failure in the speed sensor.

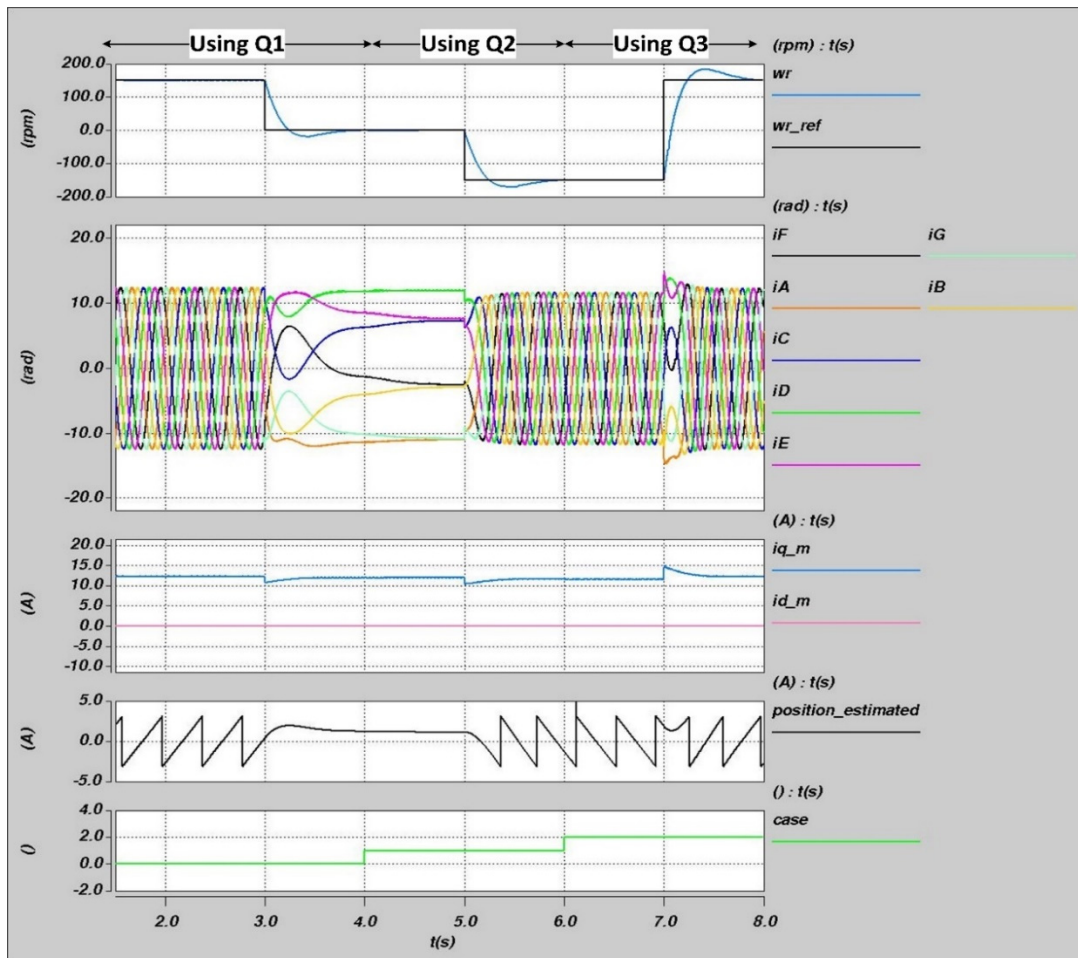


Figure 15. Sensorless speed control results.

5. Current Distortion

The main difficulty when applying current derivative-based position estimation schemes to real systems arises from the parasitic effects within the motor, the inverter, and the cabling [28]. Hence, narrow active voltage vectors must be extended to a minimum vector duration t_{min} which is set according to the high-frequency decay as shown in Figure 16a. In this paper, t_{min} was set to 8 μ s. This means that the active vectors whose dynamic response of application was used to track the saliency should be extended to t_{min} if its time duration is less than t_{min} . This will introduce a large distortion in the motor currents at low speeds, as shown in Figure 16b which was taken for a real three-phase motor. This distortion causes audible noise, torque pulsation, and increases losses.

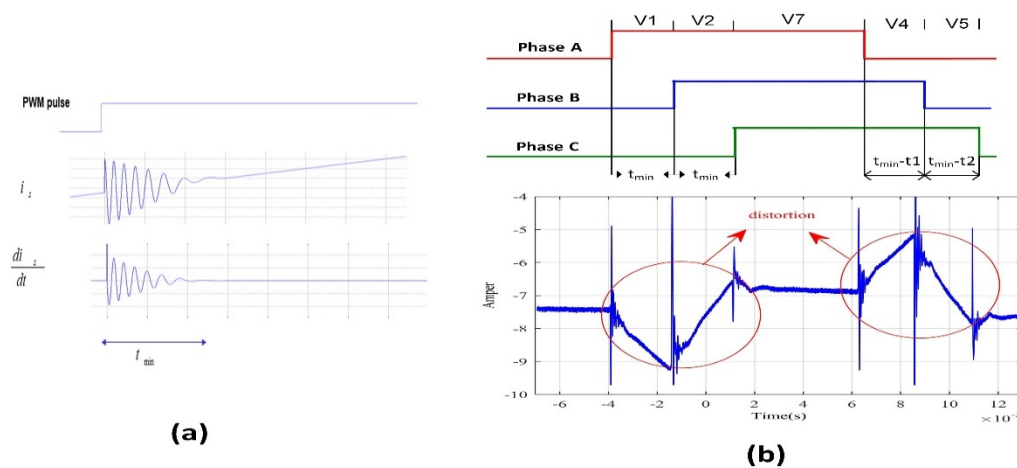


Figure 16. (a) HF oscillations when IGBT switches state, and (b) dynamic current response.

In this paper, the dynamic response of three different active vectors ($Q1$, $Q2$, and $Q3$) can be used to track the saliency, as shown in the previous section. However, when the 3rd and 5th harmonics of the reference voltages are set to zero, the time duration of the application of these active vectors will be different, as shown in Equations (13) and (14) in Figure 6. The time duration of the applications of the active vector $Q2$ will be 1.8093 times the time duration of the application of the active vector $Q1$. Moreover, the time duration of the application of the active vector $Q3$ will be 2.2524 times the time duration of the application of the active vector $Q1$. This means that it is more likely to have a time duration of the active vector $Q3$ higher than t_{min} , which means that no extension to the active vector will be needed in this case. If time duration of the active vector $Q3$ is still less than t_{min} , it will need to be extended for a further short period. In both cases, this will lead to a minimum current distortion compared to the application of the other active vectors $Q2$ and $Q1$. In the same way, it is expected to have less distortion in the current when the active vector $Q2$ is used to track the saliency since it has a longer time duration compared to the active vector $Q1$.

The above idea is demonstrated using a Saber simulator and the results are shown in Figures 16–19. In Figure 17, the motor was controlled to work at 90 rpm. In the time interval (2–3 s), there were no extensions to any vector. In time intervals (3–4 s), (4–5 s), and (5–6 s), the active vectors $Q1$, $Q2$, and $Q3$ were extended to 8 μ s, respectively, when their duration time was less than that. The signals 'count $Q1$ ', 'count $Q2$ ', and 'count $Q3$ ' are counters to count how many times the active vectors $Q1$, $Q2$, and $Q3$ are needed to be extended in simulation, respectively. It can be shown from the values of these signals that active vectors needed to be extended every PWM period (5000 PWM in each second since the switching frequency is 5 kHz). This means that all the active vectors have duration time less than 8 μ s. This can be expected since the speed is low.

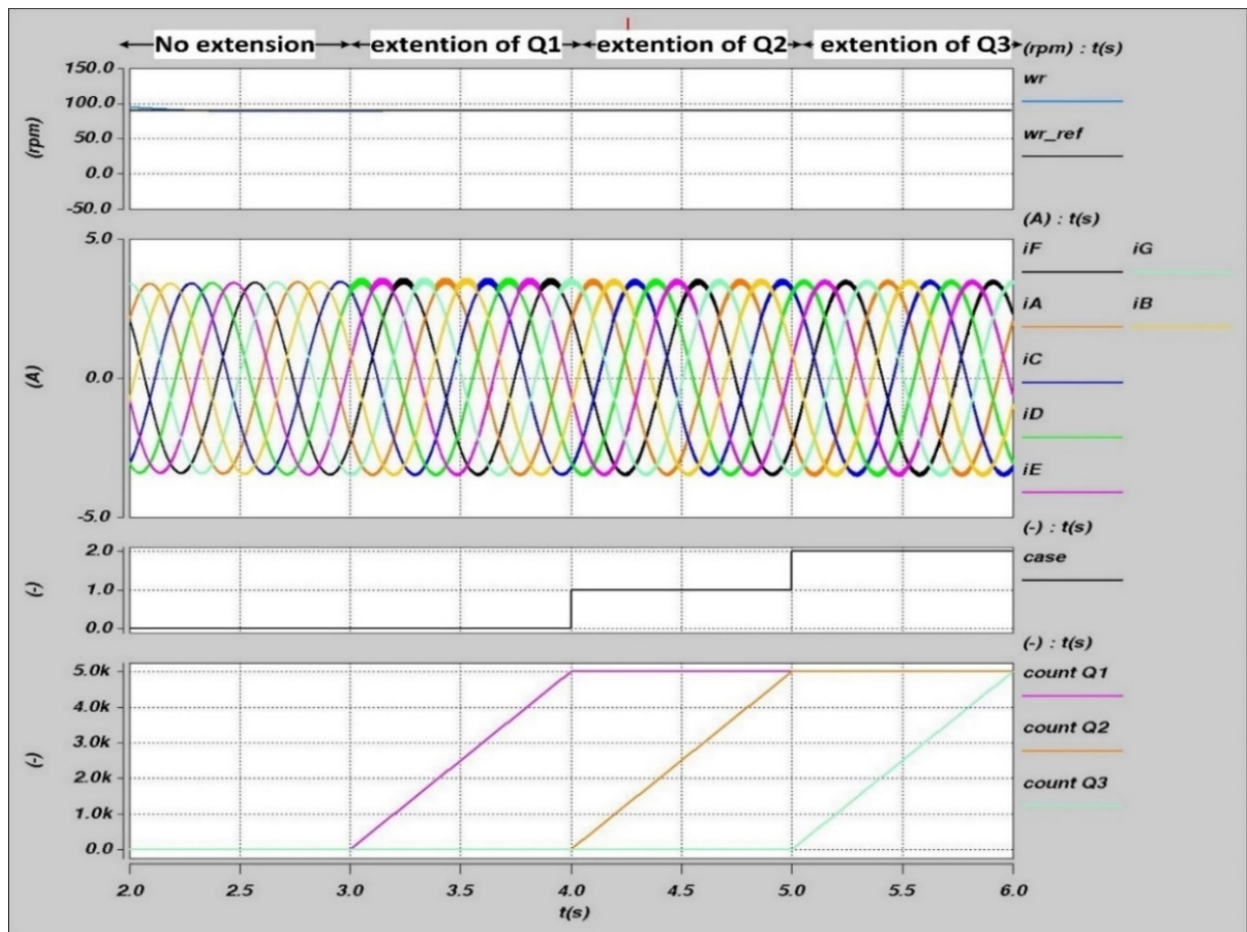


Figure 17. Current waveforms at 90 rpm using different extension schemes.

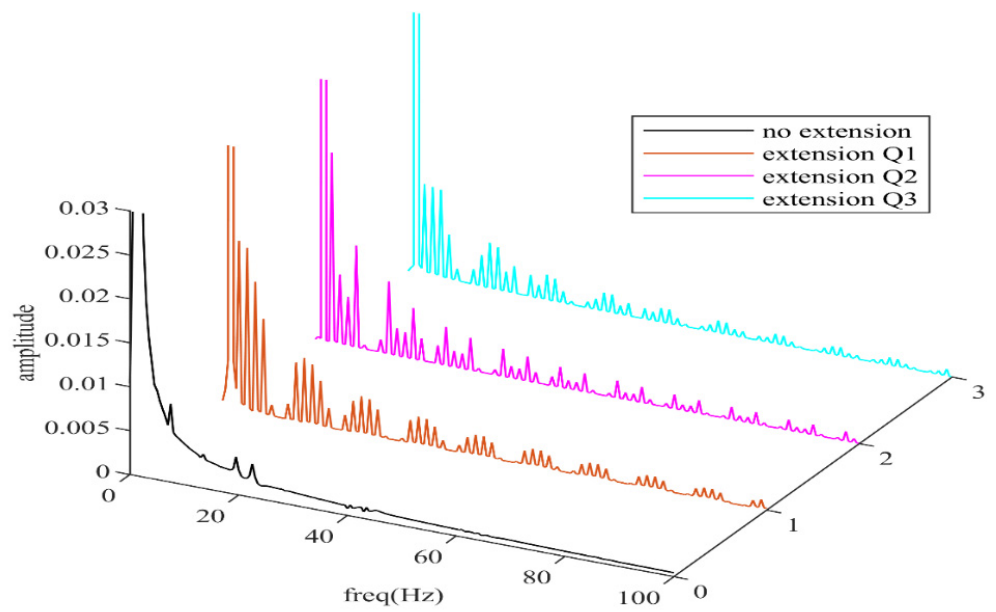


Figure 18. FFT of the current waveforms at 90 rpm using different extension schemes.

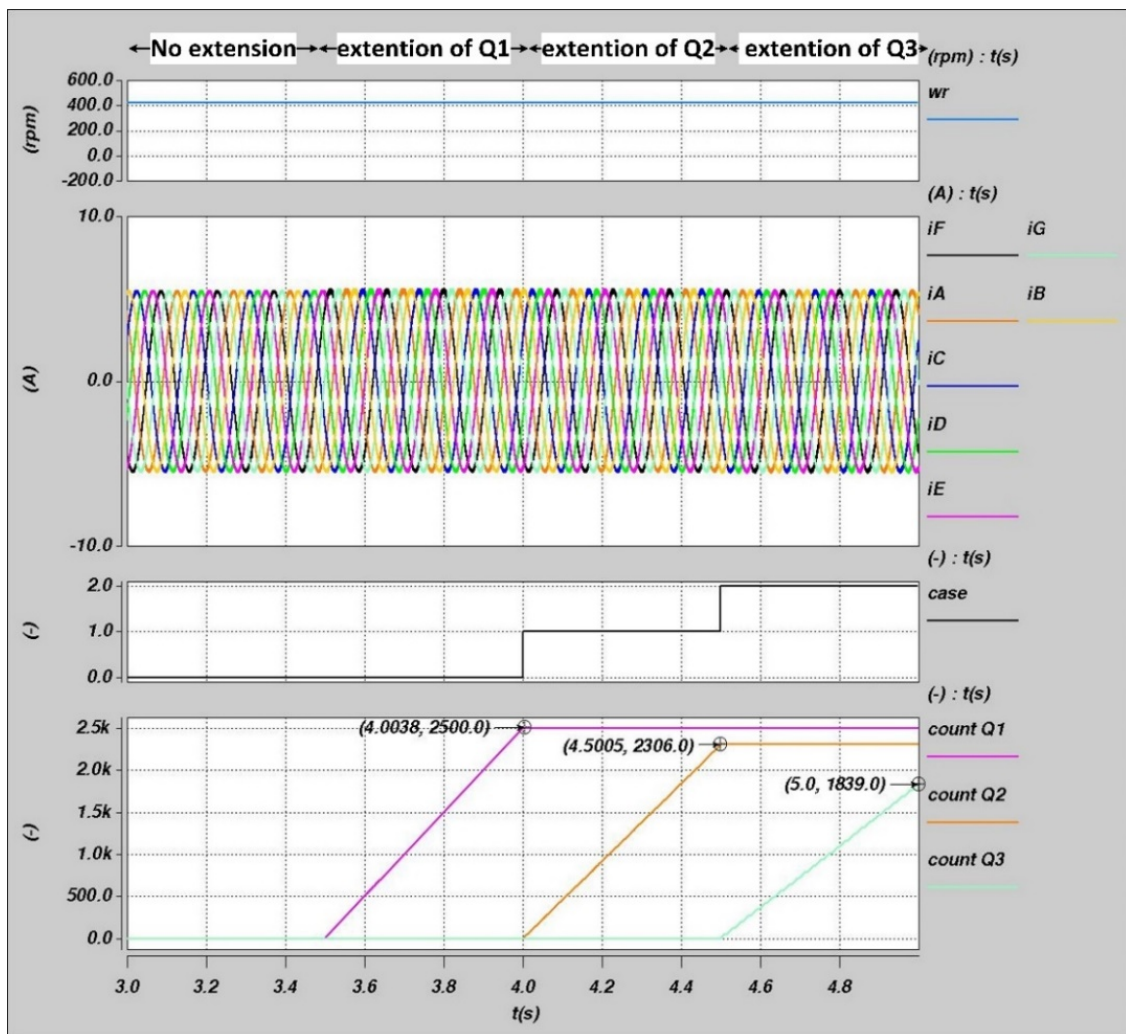


Figure 19. Current waveforms at 90 rpm using different extension schemes.

The current waveform in each time interval was further checked to see if there was a reduction in the current distortion in the case of using active vector Q3 compared to the use of the other two active vectors, Q1 and Q2. The FFT of the current at each time is depicted in Figure 18. The Total Harmonic Distortion (THD) was: 0.7% in the case of no-extension, 1.7% in the case of extension Q1 (case = 0), 1.3% in the case of extension Q2 (case = 1), and 1.05% in the case of extension Q3 (case = 3). The spectrum and the THD show that the minimum distortion occurred when the Q3 was extended, which agrees with previous findings.

A similar test was performed at a higher speed (420 rpm) and the results are depicted in Figure 19. The results show that there was a need to extend the active vector Q3 (case = 2) in the 1839 PWM period out of the 2500 PWM period, while there was a need to extend the vector Q2 (case = 1) for 2306 PWM period out of 2500 PWM period. Finally, it was required to extend the vector Q1 (case = 0) each PWM period.

The FFT of the currents in Figure 19 at each time interval is depicted in Figure 20. It can be seen that the amplitude in the harmonics was lowest in the case of extension Q3 (case = 2). The Total Harmonic Distortion (THD) was calculated to be: 0.3% in the case of no extension, 0.4% in the case of the extension of Q3 (case = 2), 0.6% in the case of the extension of Q2 (case = 1), and 0.8% in the case of the extension of Q1 (case = 0). It can be concluded from the above results that it is better to use the active vector Q3 (case = 2) to track the saliency since it gives minimum distortion in the current compared to the other vectors.

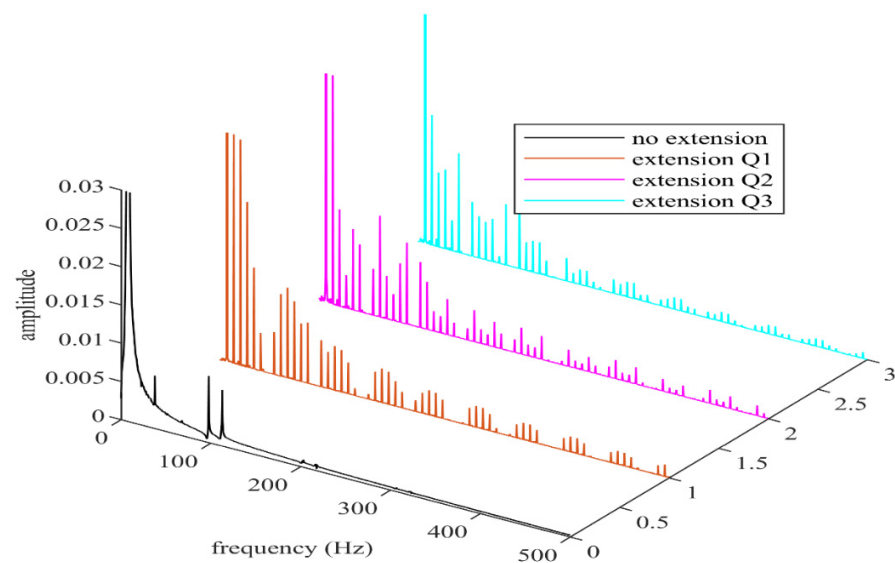


Figure 20. FFT of the current waveforms at 420 rpm using different extension schemes.

6. Conclusions

This paper has proposed three algorithms to track the saturation saliency in the seven-phase PMSM motor to perform the operation in sensorless mode. A comparison was conducted between these algorithms which showed that using the active vector Q3 (case = 2) helped to reduce the THD in the stator currents more than when using the other active vectors Q1 and Q2. This is because this active vector has a longer time duration compared to the other active vectors Q1 and Q2. This works to reduce the number of times that the active vector needed to be extended to t_{min} , hence the minimum THD. In addition, the control techniques can work at low and high speeds in a sensorless mode with performances similar to that obtained in a sensed mode. Finally, this paper recommends the use of the algorithm obtained when the active vector Q3 (case=2) achieved sensorless control for the seven-phase PMSM drive.

Author Contributions: K.S. and M.S. conceived and designed the experiments; K.S. performed the experiments; K.S. analyzed the data; K.S. contributed reagents/materials/analysis tools; K.S. and M.S. wrote the paper. All authors have read and agreed to the published version of the manuscript.

Funding: This research received no external funding.

Conflicts of Interest: The authors declare no conflict of interest.

Appendix A

The motor parameters are: rated voltage = 400 V, rated speed = 1500 rpm, rated torque = 12.N.m, rated power = 2.15 kW, $k_t = 1.2$ N.m/A, $k_e = 147$ v/Krpm, Inertia = 20 kg/cm², R(ph-ph) = 4 Ω , and L(ph-ph) = 29.8 mH

References

1. Villani, M.; Tursini, M.; Fabri, G.; Castellini, L. Multi-phase fault tolerant drives for aircraft applications. In Proceedings of the Electrical Systems for Aircraft, Railway and Ship Propulsion Conference, Bologna, Italy, 19–21 December 2010; pp. 1–6.
2. Song, Q.; Zhang, X.; Yu, F.; Zhang, C. Research on Space Vector PWM of Five-Phase Three-Level Inverter. In Proceedings of the International Conference on Electrical Machines and Systems, Nanjing, China, 27–29 September 2005; pp. 1418–1421.
3. Grandi, G.; Serra, G.; Tani, A. Space vector modulation of a seven-phase voltage source inverter. In Proceedings of the International Symposium on Power Electronics, Electrical Drives, Automation and Motion, Taormina, Italy, 23–26 June 2006; pp. 1149–1156.
4. Pradeep, J.; Devanathan, R. Comparative analysis and simulation of PWM and SVPWM inverter fed permanent magnet synchronous motor. In Proceedings of the International Conference on Emerging Trends in Electrical Engineering and Energy Management, Roorkee, India, 21–23 February 2013; pp. 299–305.

5. Casadei, D.; Dujic, D.; Levi, E.; Serra, G.; Tani, A.; Zarri, L. General modulation strategy for seven-phase inverters with independent control of multiple voltage space vectors. *IEEE Trans. Ind. Electron.* **2008**, *55*, 1921–1932. [[CrossRef](#)]
6. Zhang, D.; Xu, B.; Yang, H.; Zhu, P. Simulation analysis of SVPWM based on seven-phase permanent magnet synchronous motor. In Proceedings of the International Conference on Control, Automation and Information Sciences (ICCAIS), Ansan, Korea, 18–21 October 2017; pp. 251–256.
7. Gong, W.; Wang, Y.; Cai, Z.; Wang, L. Finding multiple roots of nonlinear equation systems via a repulsion-based adaptive differential evolution. *IEEE Trans. Syst. Man Cybern. Syst.* **2020**, *50*, 1499–1513. [[CrossRef](#)]
8. Dabour, S.M. Space vector PWM technique to reduce common mode voltage for seven-phase inverters. In Proceedings of the International Middle East Power Systems Conference, MEPCON, Al Mansoura, Egypt, 15–17 December 2015.
9. Lu, M.; Zhang, D.; Xu, B.; Yang, H.; Xin, Y. Multiphase SVPWM Strategy Analysis and Implementation of Seven-Phase Permanent Magnet Synchronous Motor. *Complexity* **2020**, *2020*, 8854472. [[CrossRef](#)]
10. Bhuiyan, E.A.; Akhand, M.; Das, K.; Ali, M.; Tasneem, Z.; Islam, M.; Saha, D.; Badal, F.; Ahamend, M.; Moyeen, S. A Survey on Fault Diagnosis and Fault Tolerant Methodologies for Permanent Magnet Synchronous Machines. *Int. J. Autom. Comput.* **2020**, *17*, 763–787. [[CrossRef](#)]
11. Mini, Y.; Nguyen, N.K.; Semail, E. A novel Sensorless Control Strategy Based on Sliding Mode Observer for Non-Sinusoidal Seven-phase PMSM. In Proceedings of the 10th International Conference on Power Electronics, Machines and Drives (PEMD 2020), Online, 15–17 December 2020; pp. 694–699. [[CrossRef](#)]
12. Fan, Y.; Deng, Z.; Wang, Z.; Li, S. Equivalent Inductance-based Flux Observer for Tri-Three-phase PMSM Sensorless Control. In Proceedings of the 2021 24th International Conference on Electrical Machines and Systems (ICEMS), Gyeongju, Korea, 31 October–3 November 2021; pp. 2537–2541. [[CrossRef](#)]
13. Fan, C.; Lu, H.; Meng, Y.; Gao, D. Sensorless Fault-Tolerant Control of Dual Three-Phase Permanent Magnet Synchronous Motor. *World Electr. Veh. J.* **2021**, *12*, 183. [[CrossRef](#)]
14. Bednarz, S.; Dybkowski, M. Induction Motor Windings Faults Detection Using Flux-Error Based MRAS Estimators. *Diagnostyka* **2019**, *20*, 87–96. [[CrossRef](#)]
15. Korzonek, M.; Tarchała, G.; Orłowska-Kowalska, T. A review on MRAS-type speed estimators for reliable and efficient induction motor drives. *ISA Trans.* **2019**, *93*, 1–13. [[CrossRef](#)] [[PubMed](#)]
16. Qin, Y.; Wang, A. Direct Torque Control of Five-phase Permanent Magnet Synchronous Motor Based on Model Prediction. In Proceedings of the 2021 International Conference on Machine Learning and Intelligent Systems Engineering (MLISE), Chongqing, China, 9–11 July 2021; pp. 126–130. [[CrossRef](#)]
17. Zhang, L.; Fan, Y.; Li, C.; Nied, A.; Cheng, M. Fault-tolerant sensorless control of a five-phase FTFSCW-IPM motor based on a wide-speed strong robustness sliding mode observer. *IEEE Trans. Energy Convers.* **2018**, *33*, 87–95. [[CrossRef](#)]
18. Almarhoon, A.H.; Zhu, Z.Q.; Xu, P. Improved rotor position estimation accuracy by rotating carrier signal injection utilizing zero-sequence carrier voltage for dual three-phase PMSM. *IEEE Trans. Ind. Electron.* **2017**, *64*, 4454–4462. [[CrossRef](#)]
19. Liu, G.; Geng, C.; Chen, Q. Sensorless Control for Five-Phase IPMSM Drives by Injecting HF Square-Wave Voltage Signal into Third HarmonicSpace. *IEEE Access* **2020**, *8*, 69712–69721. [[CrossRef](#)]
20. Saleh, K.; Sumner, M. Sensorless Speed Control of Five-Phase PMSM Drives in Case of a Single-Phase Open-Circuit Fault. *Iran J. Sci. Technol. Trans. Electr. Eng.* **2019**, *43*, 501–517. [[CrossRef](#)]
21. Elbarbary, Z.M. Salem Speed sensorless control of seven phase asynchronous motor drive system using extended Kalman filter. *Int. J. Electron. Lett.* **2021**. [[CrossRef](#)]
22. Bıçak, A.; Gelen, A. Sensorless direct torque control based on seven-level torque hysteresis controller for five-phase IPMSM using a sliding-mode observer. *Eng. Sci. Technol. Int. J.* **2021**, *24*, 1134–1143. [[CrossRef](#)]
23. Listwan, J.; Pienkowski, K. Comparison of DFOC of Seven-Phase Induction Motor with PI and Fuzzy-Logic speed Controller under speed sensor fault. *Przegląd Elektrotechniczny* **2020**, *96*, 9–13. [[CrossRef](#)]
24. Luo, Y.-C.; Huang, W.-A. Sensorless rotor field direct orientation controlled induction motor drive with particle swarm optimization algorithm flux observer. *J. Low Freq. Noise Vib. Act. Control* **2019**, *38*, 692–705. [[CrossRef](#)]
25. Mossa, M.A.; Echeikh, H.; Iqbal, A.; Duc Do, T.; Al-Sumaiti, A.S. A Novel Sensorless Control for Multiphase Induction Motor Drives Based on Singularly Perturbed Sliding Mode Observer-Experimental Validation. *Appl. Sci.* **2020**, *10*, 2776. [[CrossRef](#)]
26. Listwan, J.; Pieńkowski, K. Comparative Analysis of Control Methods with Model Reference Adaptive System Estimators of a Seven-Phase Induction Motor with Encoder Failure. *Energies* **2021**, *14*, 1147. [[CrossRef](#)]
27. Lorenz, R.D.; Van Patten, K.W. High-resolution velocity estimation for all-digital, ac servo drives. *IEEE Trans. Ind. Appl.* **1991**, *27*, 701–705. [[CrossRef](#)]
28. Hua, Y.; Sumner, M.; Asher, G.; Gao, Q.; Saleh, K. Improved sensorless control of a permanent magnet machine using fundamental pulse width modulation excitation. *IET Electr. Power Appl.* **2011**, *5*, 359–370. [[CrossRef](#)]